Delft University of Technology

MSc. Offshore and Dredging Engineering

Thesis: OE54035

Development and Application of a Novel Copula-Based Framework for Wave Energy Converter Site Comparison

Author:
Rutger Plat (4963695)

Supervisors:
Patricia Mares Nasarre, George Lavidas

September 12, 2025

Source: CorPower Ocean (2025)

TU Delft Delft University of Technology

Abstract

Pre-operational site comparison studies for Wave Energy Converters (WECs) typically do not account for potential dependencies between site selection criteria. This study addressed this gap by developing a novel copula-based site comparison framework that evaluated the trade-off between extreme loads and power production while incorporating their dependency. The results showed that dependencies may exist between these criteria and that accounting for them could improve conventional site comparison approaches. Additionally, the study was extended to an operational context, enabling operators to anticipate future operational periods with relatively high or low probabilities of failure.

The study began with a literature review to identify common site selection criteria, such as power production and wave energy variability, as well as site selection trade-offs like extreme loads and fatigue. Building on these insights, the focus was narrowed to a framework modeling the relationship between annual power production (E_0) and annual peak heave load (F_p). Subsequently, the framework was applied to three WEC deployment sites in France, Portugal, and Ireland using thirty years of wave data from the ECHOWAVE hindcast dataset. This data was fed into a power production model to calculate E_0 and a load model to estimate F_p, yielding thirty annual observed (F_p, E_0) pairs per site. At each site, parametric bivariate copulas were fitted to the (F_p, E_0) data to model their dependence and were then used to simulate 10^6 (F_p, E_0) samples per location. Probabilistic approaches were applied to compare sites based on the E_0–F_p trade-off, with F_p interpreted as probability of failure for a critical component resistance of $f_f = 3500$ kN.

The results provided evidence of statistically significant E_0–F_p dependencies in Portugal ($r = -0.34$) and Ireland ($r = 0.28$), while independence could not be rejected for France ($r = -0.10$). The opposite signs indicated that higher power production does not always correspond to higher extreme loads, providing an opportunity to use this distinction to improve conventional site comparison approaches. Probabilistic analysis of the simulated samples showed that France exhibited a much higher yearly probability of failure ($P_{\text{yearly},f} \approx 14\%$) compared to Portugal and Ireland ($P_{\text{yearly},f} \approx 3\%$), with Portugal showing higher average annual power production ($\overline{E_0} \approx 2098$ MWh) compared to Ireland ($\overline{E_0} \approx 1752$ MWh). France was therefore left out of the subsequent analysis. Focusing on the remaining two sites, high power production in Ireland corresponded with a higher probability that F_p exceeds f_f, whereas in Portugal it corresponded with a lower probability. This difference reflected the opposite correlations between E_0 and F_p in the two sites, with the negative correlation in Portugal offering potential benefits for project profitability. Finally, the operational analysis for Ireland revealed a statistically significant dependence between the first six months of production (E_1) and F_p. This indicates that the yearly probability of F_p exceeding f_f varies annually and can be estimated from the observed E_1 values, supporting more proactive maintenance scheduling.

The copula-based site comparison framework was used to estimate expected annual power production $\overline{E_0}$ and yearly probability of failure $P_{\text{yearly},f}$, positioning it as a potential alternative to conventional pre-operational site comparison approaches focused on power production and extreme loads. In addition, the results suggested that F_p–E_0 dependence can be opposing across sites, as high power production did not necessarily coincide with higher extreme loads, which could have consequences for project profitability. Because this insight is not captured by conventional site-comparison approaches, incorporating F_p–E_0 dependence could improve these conventional approaches. Finally, the operational application showed that modeling the E_1–F_p dependency could support more effective maintenance scheduling.

Preface

This thesis was written as part of the Offshore and Dredging Engineering master track with the specialization in renewable energy at Delft University of Technology. The work was carried out between February and September 2025.

The objective centered around developing and applying a novel copula-based framework for pre-operational site comparison for wave energy converters (WEC), with the goal of laying the groundwork for future studies focused on accounting for dependencies between site selection criteria. The framework is applied to a Corpower C4 inspired WEC. The results are illustrative only and should not be considered representative of the true device.

I would like to express my gratitude to Patricia Mares Nasarre and George Lavidas for their intensive involvement and guidance throughout this project, which enabled me to achieve my objective of developing and applying a novel site-comparison approach. I am grateful to Delft University of Technology for the many learning opportunities it has offered me, and I am pleased that the knowledge and experiences gained over these years are reflected in this thesis and its process.

Contents

1 Introduction

The urgent need to lower carbon emissions and ultimately fighting climate change is what is driving the global energy transition. Fossil fuels, which now account for the majority of the world's power production (Energy Institute, KPMG, and Kearney, 2024), are a major contributor to greenhouse gas emissions, which raise temperatures, cause extreme weather, endanger human health, cause species extinction, and increase drought (United Nations, 2025).

Azam et al. (2021) estimated that the global energy demand will have risen with 11.6 times by 2050 compared to 1950 and The UN Environment Program shows that globally, we are on track to produce more than double the amount of coal, oil and gas by 2030 than we can burn if we are to limit global warming by 1.5°C (United Nations Environment Programme (UNEP) and Partners, 2019). The need for renewable energy sources to protect our environment is thus more important than ever. In 2023 the EU set a goal for reducing the net greenhouse gas emissions by at least 55% by 2030 (European Commission, n.d.) and with 90% by 2040 (European Commission, 2024). Achieving these ambitious targets will require a fundamental shift to renewable energy solutions.

The European Commission's main target is to reach 300 GW of offshore wind and 40 GW of ocean energy capacity by 2050 as part of the European Green Deal (Norton Rose Fulbright, 2020). To meet these objectives, nearly €800 billion will be needed between now and 2050, covering investments across all offshore energy solutions (European Parliament, 2020). Ocean energy is an attractive solution because it is a largely untapped renewable ocean energy resource, it offers a reliable and renewable source of energy reducing fossil fuel dependence. The Intergovernmental Panel on Climate Change (IPCC) estimates that the annual global wave energy potential is approximately 29,500 TWh/yr, of which the wave energy potential off the coasts of Eastern and Western Europe is about 2,800 TWh/yr (Intergovernmental Panel on Climate Change, 2012). This is comparable to Europe's total electricity consumption in 2023, recorded at 2,697 TWh/year (Ember, 2024). According to (Cruz, 2007; Mustapa et al., 2017; Wahyudie et al., 2017; Mork et al., 2010), between 10% and 20% of the total energy potential can be subtracted, which is a substantial amount compared to the global energy demand.

The €800 billion investment in ocean energy will ultimately increase the installed capacity of wave energy, resulting in a wide range of environmental, economic, and social benefits. These are: (i) the European Commission estimates that ocean energy could generate up to €53 billion per year in global market value, (ii) it is projected to create 400,000 jobs by 2050, (iii) it has limited environmental impact, and (iv) it contributes to the decarbonization of Europe's industries and citizens living in coastal regions (Ocean Energy Europe, 2020). In addition to these advantages, wave energy also offers several technical benefits, as it is more predictable and less volatile than wind and solar power (Energy Club TU Delft, 2025). One of the major challenges in integrating renewable energy into the grid is short-term forecasting, as it helps manage fluctuations in supply and demand (Reikard et al., 2015). Wave energy converters can produce energy up to 90% of the time, wind and solar on the other hand are only capable of producing energy 20-30% of the time (Barua and Rasel, 2024). Due to its high predictability and low volatility, integrating wave energy with solar and wind can enhance the stability of the overall energy supply and ultimately balance Europe's electricity grid (Ocean Energy Europe, 2020).

Despite wave energy's benefits its commercial utilization remains very limited (Aderinto and Li, 2018; Barua and Rasel, 2024). This is due to several technical and non-technical challenges (Guo and Ringwood, 2021), including high operational expenditures, as wave energy converters require significant installation, operational, and maintenance costs, making them financially demanding. Additionally, extreme sea conditions induce a high risk of failure and device loss, leading to an unattractive investment landscape for potential stakeholders. While these are among the key challenges facing the sector, additional barriers exist. However, considering the scope of this research, further challenges are not discussed.

Further analyzing the cause of these financial challenges, Coe et al. (2021) highlights that an increase in

average annual power production can lead to higher operational and maintenance costs due to the need to counteract increased fatigue levels. Besides cost challenges, power production efficiency is equally important. Different locations present varying conditions, resulting in differences in power production and overall operating efficiency (Coe et al., 2018).

To improve the global commercialization of wave energy, financial challenges must be addressed. Improved site comparison can play a key role in balancing low operational expenditures with high annual power production, ultimately enhancing commercial viability. This research aims to develop and apply a copula-based framework used to support pre-operational site comparison, considering trade-offs between device performance and factors that could ultimately effect costs of wave energy projects. As Coe et al. (2021) insightfully states: "As a wise engineer once said, 'there is no free lunch.' Every benefit comes with some finite cost. The balancing of these finite benefits and costs is, perhaps, the essence of engineering design. The benefit of capturing the most powerful ocean waves may not be worth the cost."

Wave energy performance studies and resource studies are conducted to analyze the specific conditions at each potential site and to compare them to ultimately find the most suitable site. These site comparison studies typically assume independence between selection criteria, neglecting the relationship between criteria may lead to overlooking factors that could have influenced site comparison assessment if they were taken into account.

To address this gap, this study aims to explore the potential added value of taking the relationship between site selection criteria into account. In order to achieve this, Copulas, mathematical models for the dependence between variables, offer a flexible and promising approach to better assess the key criteria for each location. While Copula models have been applied in various ocean engineering studies, their application to WEC site comparison remains largely unexplored, this presents a unique opportunity to explore its potential.

This research is structured in two main parts. The first part is the literature study, where the copula-based framework is developed to support pre-operational site comparison for a device inspired by the CorPower C4 (CorPower Ocean, 2025), based on a trade-off between power performance and manageable loads while taking their dependency into account. The second part applies the developed framework to three locations to demonstrate how it could improve or replace conventional pre-operational site-comparison assessments. These objectives lead to the following two research questions:

1. **Literature Study:** What copula-based framework can be developed to support pre-operational site comparison for a device inspired by the CorPower C4, based on a trade-off between energy performance and manageable loads?
2. **Main Thesis:** How could the developed copula-based framework be used to improve or replace conventional pre-operational site comparison assessments?

2 Literature Study

In order to construct a copula-based framework that supports pre-operational site comparison and ultimately addresses the literature study objective, the literature study is organized into five research areas. Subsection 2.1 addresses general site selection criteria, where resource and WEC-specific performance studies are analyzed to build a thorough understanding of all criteria relevant to the pre-operational site comparison. Subsection 2.2 investigates site selection trade-offs relevant to the commercial viability of wave energy converter projects, particularly those associated with operational and extreme loads. Subsection 2.3 narrows down the site selection criteria and trade-offs discussed in Subsections 2.1 and 2.2, ultimately presenting the final framework. Finally, Subsection 2.4 presents the motivation behind the final framework, whereas Subsection 2.5 describes the device characteristics and the kind of dataset utilized in this research.

2.1 General Site Selection Criteria

The most widely recognized criteria for determining site suitability can be categorized into three main criteria: (i) wave energy resource, (ii) power production, and (iii) extreme events, depicted in Figure 1. In literature, each of these criteria is assessed using different methodologies. Wave energy resource refers to the availability and consistency of wave energy at a given location, which is typically quantified using energy flux and pre-production metrics such as the coefficient of variation (CoV). Power production focuses on efficiency and how much power is ultimately produced by a WEC, for which post-production metrics are often applied. Extreme events are generally assessed using the return period wave, which represents the wave height statistically expected to be exceeded once within a specified return period, such as 50 years. This subsection reviews the three general site selection criteria, highlighting their importance and the ways in which they are applied across different studies.

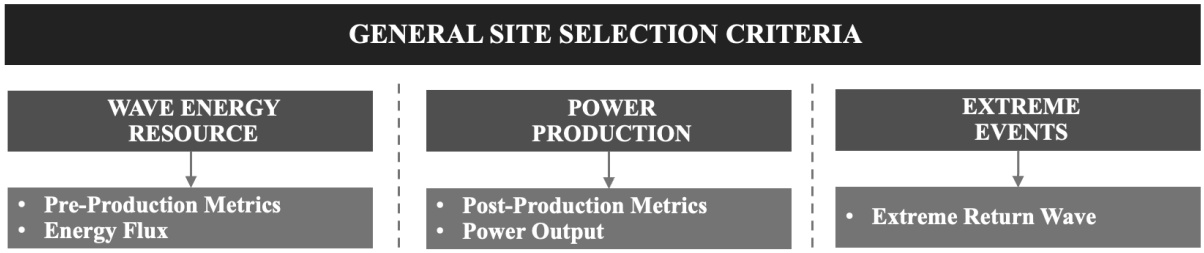

Figure 1: General site selection criteria identified from WEC studies

2.1.1 Wave Energy Resource

Site selection criteria focused on the wave energy resource evaluate the available wave energy without focusing on any specific device. The wave resource is often described as wave flux or wave energy density (kW/m), it tells how much energy is available for extraction. Besides wave power density, wave variability is a major factor in resource assessments, incident wave conditions at any site are highly variable, fluctuations occur within an individual wave cycle all the way up to seasonal and annual changes (Orszaghova et al., 2022). In literature, wave variability at the resource level is often quantified using pre-production metrics. The reason that variability is an important factor is that variability has a large influence on the overall performance of a WEC. Multiple studies, such as Coe et al. (2021) and Reguero et al. (2015), focus on identifying suitable locations for WEC deployment through resource assessments that highlight areas with high wave energy potential and low seasonal or inter-annual variability. While wave energy flux and pre-production metrics provide a valuable initial assessment, it does not indicate WEC performance. Given that this study focuses on a particular device, resource-level assessments are of lesser importance.

2.1.2 Power Production

Site selection criteria focused on power production and are often expressed in the literature in the form of post-production metrics or power output. Some studies calculate power output or its variability directly like Orszaghova et al. (2022), while others use normalized metrics to enable comparison of different devices across sites (Lavidas, 2020; Choupin et al., 2022; Lavidas, 2020; Lavidas et al., 2021; Bozzi et al., 2014). From these studies, two main approaches to assessing the power output and variability of a WEC can be distinguished: one focuses on comparing multiple WECs across multiple sites using normalized post-production metrics or indices, while the other concentrates on a single WEC at a limited number of locations, where power output and variability are evaluated more directly without necessarily relying on post-production metrics.

2.1.3 Extreme Events

Extreme events in wave energy occur when wave height (and associated wave period) exceed a established threshold, often due to storms or seasonal variations. There is a number of technical issues when deploying a WEC but the resistance to extreme wave loads is within the most challenging ones (Vannucchi and Cappietti, 2016). These events lead to heavy structural loads on the WEC, increasing the probability of failure (Santo et al., 2020) and ultimately leading to higher maintenance costs, downtime or loss of device (Aderinto and Li, 2018). Due to the significant challenges associated with extreme sea conditions, they are often considered when determining site suitability. For this reason, extreme events are categorized as a "general site selection criteria" in this research. However, they can also present a trade-off: A WEC may produce stable and efficient power output at a site but be exposed to severe extremes, which will demand more robust mooring systems. This increases capital expenditures and can ultimately reduce the project's economic viability. Due to this overlap between general site selection criteria and site selection trade-offs, the approaches used to assess extreme events at each site will be further discussed in the Section 2.2.

2.2 Site Selection Trade-Offs

Subsection 2.1 highlighted the various approaches used to assess site suitability for WEC deployment. Once a specific design is chosen, the focus typically shifts to WEC-specific performance studies, focusing on power production, efficiency and production stability, which are three key criteria for evaluating device performance. However, beyond these primary criteria, structural risks should also be considered. While high-energy sea states offer greater power potential, they often come with (i) increased structural loads, (ii) higher degradation rates, (iii) and exposure to extreme environmental conditions (Thies et al., 2014). These factors can lead to accelerated fatigue, increased maintenance costs, potential operational downtime and loss of device, ultimately impacting the long-term viability of the project (Ferri et al., 2014). To ensure a balanced and cost-effective deployment, it is essential to evaluate trade-offs between device performance and other factors associated with structural risks. Multiple studies focused on trade-offs in offshore floating wind (OFW) and wave energy were reviewed. These studies ultimately served as inspiration for developing a overview of all potential site selection trade-offs in wave energy. Floating wind studies were analyzed, as offshore wind benefits from a more mature industry, standardized designs leading to extensive studies on degradation and extreme conditions. In contrast, wave energy converters are still in the pre-commercial phase, with diverse designs and fewer deployments. The following Subsections 2.2.1 and 2.2.2 provide an overview of the main site selection trade-offs discussed in these studies.

2.2.1 OFW and WEC Studies

In short, OFW studies (Zhao and Dong, 2023; Winterstein et al., 1993; Yuan et al., 2024; Li and Zhang, 2020b) emphasize fatigue and extreme load calculations as key criteria for assessing site suitability and struc-

tural risks. WEC studies address similar issues, though within a less mature and more diverse technological landscape. For example, Shahroozi et al. (2022) determined the design loads for mooring line forces based on extreme conditions. Likewise, Katsidoniotaki et al. (2020) focuses on a point-absorber that is moored to the seabed with a single mooring line. After determining the design load, a reliability assessment is conducted, aiming to quantify the probability of failure for a critical component under extreme conditions. Beyond survivability, operational conditions were addressed by Abaei et al. (2025), who developed a performance evaluation framework combining power output and structural reliability. Similarly, Paduano et al. (2024) proposed a standardized design approach using high-fidelity models, considering both peak loading under extreme conditions and damage accumulation under operational conditions, while also emphasizing trade-offs between energy performance and structural reliability. Paduano et al. (2024) seeks to develop a standardized design approach using high-fidelity models, considering both operational and extreme conditions. For extreme conditions, the focus is on assessing peak loading, while for operational conditions, the authors perform an actual damage calculation.

2.2.2 Site Selection Trade-Offs Categorization

Figure 2 presents the site selection trade-offs identified in both WEC and OFW studies, categorized as operational or extreme conditions. Since both conditions are important, their combination could offers a comprehensive approach to site assessment. For extreme conditions, the focus is on survivability, evaluating whether the peak force in the selected critical component exceeds the resistance of the system. Additionally, if the system's resistance and extreme load distribution can be determined, its reliability can be assessed. In contrast, for operational conditions, the emphasis shifts toward fatigue, examining the long-term effects of cyclic loading on a critical component. For each of these areas, a specific critical component is selected. Across studies (Tom, 2022; Guo et al., 2022; Abaei et al., 2025), the following components are labeled as "critical": (i) Mooring lines/fairleads/connections, responsible for station-keeping and resisting cyclic wave loads, (ii) PTO system, which converts wave energy into usable power and is subject to mechanical stresses, (iii) the hull of the buoy that must withstand hydrodynamic forces and environmental exposure.

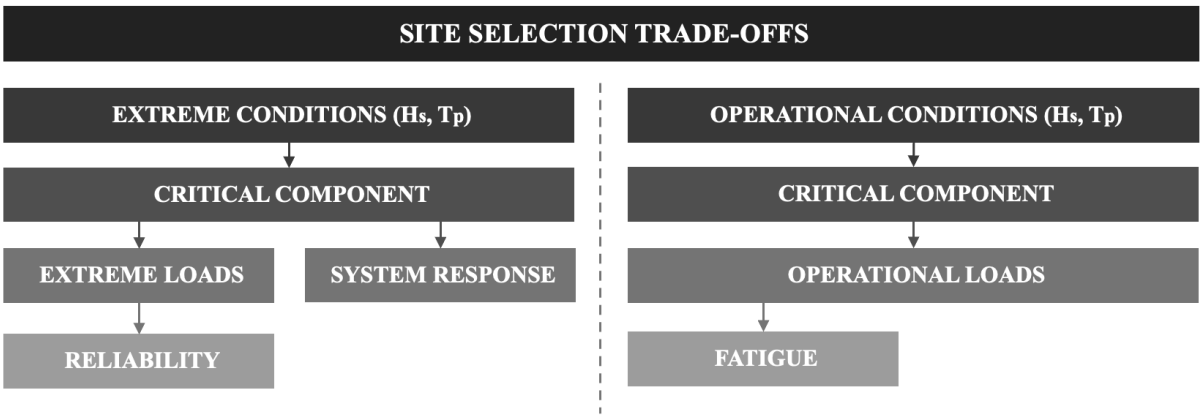

Figure 2: Site Selection Trade-offs identified from WEC and OFW studies

In summary, site comparison requires balancing between power production and structural risks under both operational and extreme conditions. Which of the site selection trade-offs in Figure 2 are evaluated in the final copula-based site comparison framework of this study depends on the level of detail required, computational costs, time constraints, and resource availability, which are discussed further in the following Subsection 2.3.

2.3 Final Copula-Based Site Comparison Framework

Figure 3 shows the final copula-based site comparison framework. The framework addresses the trade-off between power production and extreme loads. The left side of the framework focuses on the calculation of the annual peak heave load F_p exerted on the braking system in extreme conditions, while the right side focuses on the calculation of the annual power production E_0 over that same period. The fitted copula models the dependence between F_p and E_0, and it enables the simulation of samples in which each sample represents a pair of F_p and E_0. From these simulated samples, probabilistic approaches can be utilized to compare sites based on a trade-off between power production and extreme loads.

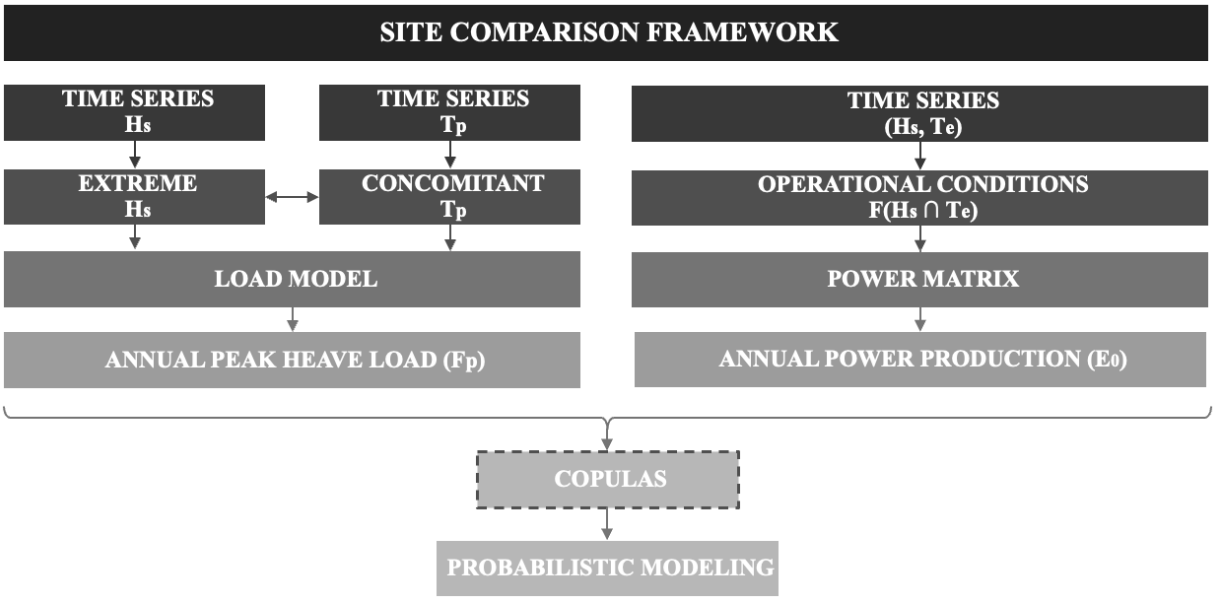

Figure 3: Final copula-based site comparison framework

The following subsections provide an initial overview of the steps within the final framework. Subsection 2.3.1 introduces the approach for determining E_0, while Subsection 2.3.2 explains the approach for determining F_p. A more detailed explanation of these steps is provided in Sections 3 and 4.

2.3.1 Annual Power Production

The sea states corresponding to operational conditions are established using methods consistently utilized in wave energy studies (Carballo and Iglesias, 2012; Nicolas Guillou, 2018; Orszaghova et al., 2022). This approach produces a scatter diagram represented by the function $F(H_{s_{i,j}} \cap T_{e_{i,j}})$, which describes how frequently (or what fraction of time) different combinations of significant wave height $H_{s_{i,j}}$ and energy period $T_{e_{i,j}}$ occur based on empirical (H_s, T_e) time series extracted from the dataset. Only wave heights that fall within the operational boundaries are considered as operational conditions. The expected power production of the WEC is then determined using the power matrix. This matrix uses the operational conditions defined by the wave scatter diagram $F(H_{s_{i,j}} \cap T_{e_{i,j}})$ as input to compute the expected power production for a chosen time step ΔT. In this study, an existing power matrix for a CorPower C4-inspired wave energy converter is used.

2.3.2 Annual Peak Heave Load

The univariate distributions of sea states for extreme conditions are first characterized applying Extreme Value Analysis for both wave height H_s and period T_p, being H_s the dominant variable. Using the Peak Over Threshold method, the highest values of H_s values are selected from the wave height time series. The concomitant T_p value is sampled from the wave period time series; this is, the value of T_p that occurs at the same time as the extreme H_s. This yields the highest observed wave height and wave period pairs (H_s, T_p). The extreme values of wave height H_s and period T_p will be input for the load model, in this model the peak heave load F_p associated with the estimated extreme wave will be determined.

2.4 Copula-Based Site Comparison Framework Motivation

This Subsection combines the insights from Sections 2.1 and 2.2, which respectively examined (i) general site selection criteria and (ii) site selection trade-offs. Ultimately, explaining why certain general site selection criteria or trade-offs are within (or not) the framework depicted in Figure 3. The options considered for general site selection criteria are illustrated in Figure 1, while those related to site selection trade-offs are shown in Figure 2. Throughout this Subsection the general site selection criteria and trade-offs are evaluated according to the four topics listed below, if a general criteria or trade-off does not meet one of these topics, it is excluded from the framework. The topics are ranked from one to four based on importance. It is worth noting that flexibility ranks second because the framework should be flexible to adapt to changes in scope. If time allows, it should be possible to easily extend, but it must also be possible to cut back if certain aspects turn out to be unfeasible. This adaptability is essential for maintaining progress under uncertain or evolving conditions. Furthermore, computational feasibility is the third criteria because on one hand, modeling tools and resources such as BEM-based toolboxes for WECs are available. On the other hand, if time-domain results are needed, the simulations can take too long to be practical. Finally, uncertainty is ranked lowest, as this study aims to demonstrate the framework in practice and show its added value. Due to the limited time, this required simplifications in the F_p calculations.

1. **Relevance to Research Objective:** Does the parameter support the objective of this study?
2. **Flexibility:** Will including this parameter allow the framework to be adapted or expanded later (e.g., to include fatigue analysis or extreme scenarios)?
3. **Computational Feasibility:** Can the parameter be modeled with available tools, data and time?
4. **Uncertainty:** How robust is the parameter to variability or uncertainty in environmental data or model assumptions?

Subsection 2.4.1 explains the motivation behind the inclusion or exclusion of site selection criteria and trade-offs in the final framework. The selected critical component is presented in Subsection 2.4.2, while Subsections 2.4.3 and 2.4.4 describe how operational and extreme sea states are modeled and applied as inputs for calculating F_p and E_0.

2.4.1 Extreme Loads vs Power Production

General site selection criteria depicted in Figure 1 came down to three assessment areas being (i) wave energy resource, (ii) power production, (iii) extreme events. Extreme events are considered both as part of these general site selection criteria and within the trade-offs. The first step is to determine which of these general site selection criteria should be included in the final framework. As described in Subsection 2.1.1, pre-production metrics and energy flux provide valuable insights focused on the wave energy resource

for broad site screening. However, they are not device-specific and do not capture how a particular WEC performs. Given that this study's objective is to evaluate WEC performance, the final framework will focus on power production rather than the wave energy resource.

When evaluating the relevance of each site selection trade-off shown in Figure 2, operational conditions are important within the scope of this research, as the power production of the WEC takes place under these conditions. However, calculating loads in operational conditions may be too computational intensive intensive as it would require many time-domain simulations. Extreme conditions, on the other hand, are less time consuming to evaluate and represent one of the main barriers to the commercialization of wave energy. They are therefore highly relevant for assessing suitable deployment locations and are directly linked to the research objective of this study. Therefore, focusing on extreme loads provides a practical way forward, as it balances computational feasibility with the need for meaningful insights, requiring calculations for only a single extreme wave within a given period, such as monthly or yearly. Modeling the copula between extreme loads on the critical component and the associated power production offers the opportunity to analyze dependencies that might not be immediately apparent.

2.4.2 Braking System as Critical Component

The critical components of a WEC include the PTO system, the mooring lines, the hull, and the braking system. In OFW applications, the mooring system is typically the primary component of interest due to the large restoring forces it must induce. However, in WECs, the restoring forces required are significantly lower, making the mooring system less critical from a design perspective. Additionally, calculating the loads in mooring lines is computationally intensive, which makes them less practical to focus on in the analysis. Furthermore, a review of the literature did not identify the hull as a commonly cited critical component for WEC fatigue or failure. Notably, the PTO is subject to long-term degradation under operational conditions, and its braking mechanism must be capable of withstanding substantial loads during extreme events. Multiple researchers (Abaei et al., 2025; Guo et al., 2022; Ferri et al., 2014) consistently emphasize the significance of accurately understanding and modeling the fatigue behavior and reliability of PTO systems. According to the authors, it is essential for the commercial feasibility of WECs. This consensus justifies selecting the PTO as a critical component. However, since the final framework focuses on extreme loads, the PTO is not directly subjected to these conditions, as survival mode is typically activated. In survival mode, the braking system absorbs the extreme loads and protects the PTO. For this reason, the braking system is selected as the critical component on which F_p is applied.

2.4.3 Operational Sea State Estimation

For the power production, the scatter function describes the operational sea state used as input for the power matrix to calculate E_0. Each bin of the scatter plot represents the occurrence frequency of specific sea states defined by H_s and T_e. The power matrix corresponds to these bins, providing power output values that can be multiplied by the bin frequencies to calculate E_0. This is necessary because the power matrix consists specific bin intervals of H_s and T_e, but the available data often does not match these intervals. As a result, direct calculation of E_0 from the wave data requires interpolation. However, interpolation methods can introduce significant inaccuracies in the estimates. It is therefore more practical to use the scatter plot, which bins the data to match the power matrix intervals.

2.4.4 Extremes Sea State Estimation

There are two options for modeling extreme sea states: (i) bivariate, and (ii) univariate approach. Option (i) is a bivariate approach. In this option, a joint distribution of (H_s, T_p) is estimated and used as input

to construct the environmental contours. From these contours, extreme sea states for a given return period are estimated. Option (ii) is a univariate approach. In this case, H_s is determined using the peak over threshold (POT) method, and the concomitant T_p is sampled based on the timing of the extreme H_s. From literature no clear conclusion is drawn which method is most accurate in determining maximum wave height H_s. However the bivariate approach is widely used in offshore engineering because both the maximum peak period T_p and wave height H_s are needed in pairs. If both of these maximum values were estimated using the POT method the maximum wave height H_s will not match the wave period T_p. However, when the wave height H_s is estimated using the POT method and its concomitant wave period T_p is sampled, accurate results are obtained. In this way the POT method can still be used to estimate pairs of extreme wave height and period. Because of its simplicity and maintained accuracy due to sampling the concomitant T_p, this method will be utilized in the final framework.

2.5 Device and Wave Data

2.5.1 Device Description

A point absorber inspired by the CorPower C4 serves as the device of interest for applying the copula-based site comparison framework. The device moves up and down with the waves, the PTO system transforms this movement into power. It operates for wave heights between $0.5m$ and $10.5m$. Despite the existence of numerous WEC designs, commercial success has yet to be achieved. This is primarily due to two costly challenges: efficiency and survivability (Aderinto and Li, 2019; Zhou et al., 2024). A key feature the core power C4 has is its capability of adapting its response in varying sea conditions (Hals et al., 2016). The system's survivability is improved by its detune storm protection state. When large waves occur, the internal pressure within the system increases, preventing the buoy from moving excessively with the waves. This mechanism is comparable to how a wind turbine pitches its blades in high wind speeds. In terms of efficiency, the buoy captures energy as it ascends with the waves. As it rises, energy is stored in internal springs, which then generate a returning force as the buoy moves downward. This design allows the device to capture energy throughout the entire wave cycle, rather than just during the upstroke (Marinis, 2023/2024). When the waves become too large for the system to operate, the WEC activates a braking mechanism that restricts the buoy's vertical motion. This protects the PTO system from potential damage. The pre-tension mooring system allows the buoy to pull itself towards the ocean floor in order to keep moving in phase with the waves, maximizing efficiency.

2.5.2 Wave data and Location

In this research, the ECHOWAVE hindcast (Alday and Lavidas, 2024) is used to obtain wave data for input into the framework. This dataset was developed using WAVEWATCH III (Tolman, 1989). The hindcast is designed to provide reliable sea state characterizations for wave energy applications and is available along the entire European Atlantic coast. It has a spatial resolution of approximately 2.3 km and covers a duration of 30 years. The dataset is long-lasting, uniform, and gap-free, making them suitable for the chosen framework. The framework will be applied to conduct assessments at three sites, located in Portugal, Ireland, and France. The specific coordinates of each site are presented in Table 1.

Location	**Longitude (°)**	**Latitude (°)**
France	-8.38	47.50
Portugal	-13.75	39.75
Ireland	-9.61	52.78

Table 1: Site location and associated coordinates

2.6 Literature Study Summary

This literature study reviewed general site selection criteria and trade-offs used in WEC site comparison studies. The final copula-based framework for pre-operational site comparison was developed by narrowing the focus to E_0 and F_p and modeling their relationship with a copula. E_0 is a main driver of wave energy project success, while F_p affect commercial viability, as they can cause heavy structural loading, higher maintenance costs, downtime, or even device loss. Operational loads and fatigue are also important, but their computational intensiveness places them outside the practical scope of this study. By focusing on extreme conditions, the framework balances computational feasibility with meaningful insights. The braking system was selected as the critical component due to its role in survival mode under extreme events, and the application of copulas introduces a novel way of capturing dependencies between E_0 and F_p that conventional site comparison approaches cannot reproduce. In the following sections, the framework is applied to three sites to explore how this novel approach can improve or replace conventional site comparison approaches.

3 Power Production

This research demonstrates the practical application of the copula-based site comparison framework, which assesses site suitability by analyzing the dependency between annual power production E_0 and peak heave loads F_p. As indicated in Figure 4 this section focuses solely on the E_0. Subsection 3.1 describes the methodology for determining E_0. Subsection 3.2 elaborates on the computations and presents the associated results.

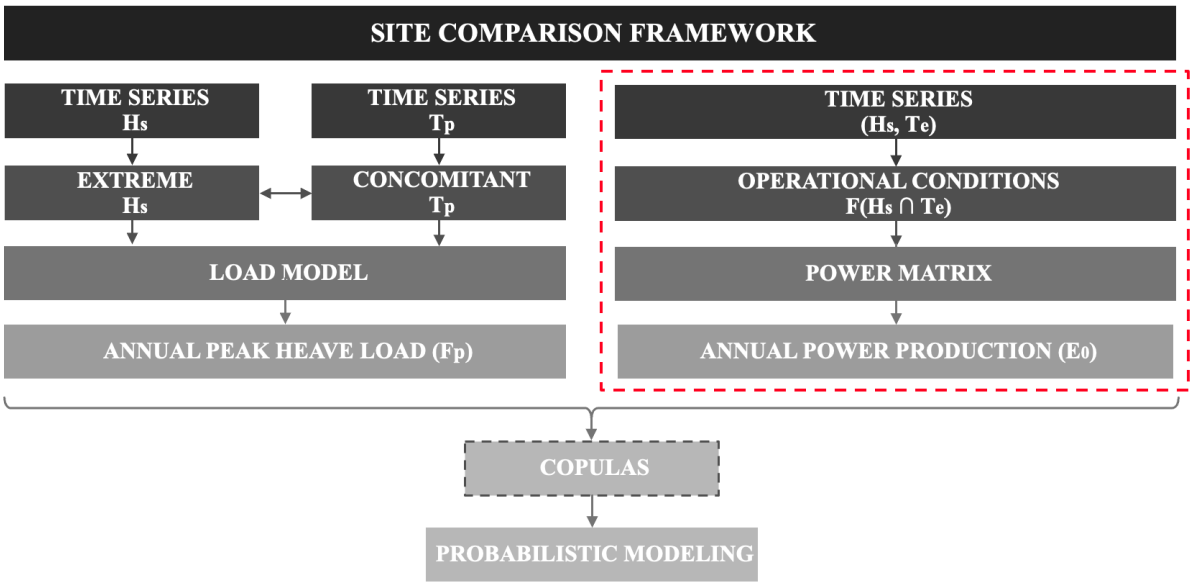

Figure 4: Copula-based site comparison framework, Section 3 focuses on the right-hand "Powery Production" branch (in red) which feeds E_0 into the copula model.

3.1 Methodology

Equation 1 gives the formulation to estimate the energy produced by a WEC, relying on the scatter function $F(H_{s_{i,j}} \cap T_{e_{i,j}})$ which represents the probability of occurrence of each sea state combination (H_s, T_e). The WEC power matrix $PM_{i,j}$ represents equivalent power curves by mapping the energy output across various wave heights and energy periods. Each bin of the power matrix defines the energy output of the WEC for a certain sea-state combination (H_s, T_e). Multiplying those terms by the time step ΔT yields the total energy produced over a given period. In this subsection the methodology used for constructing the joint probability scatter function and the corresponding power matrix is outlined.

$$E_0 = \sum_{i=1}^{n_{T_e}} \sum_{j=1}^{n_{H_s}} F(H_{s_{i,j}} \cap T_{e_{i,j}}) \cdot PM_{i,j} \cdot \Delta T \tag{1}$$

3.1.1 Power Matrix

This research builds on the PM developed by Alday et al. (2023). The PM describes the power production of the Corpower-inspired WEC for each sea-state bin. How the power production values for each bin were determined by Alday et al. (2023) is explained in Appendix G.

3.1.2 Power Matrix Reduction

In Section 4, extreme sea states are identified and used as input for the load model, which ultimately calculates F_p. This load model calculates F_p under a "survival mode" scenario, meaning the WEC is not operating and is kept fixed in the water to protect its PTO system. To obtain at least one F_p per year, the WEC must enter survival mode at least once annually. However, with the PM cut-off wave height set at 10.5 m, the WEC does not enter survival mode at some locations, making the framework inapplicable. To allow the framework to compare a wider range of locations, the PM cut-off wave height is reduced so that the device stops operating at lower wave heights. The capacity factor, shown in Equation 2, quantifies how efficiently the WEC operates over time. Here P_0 is the WEC rated capacity and E_0 is its power production. The C4-inspired CorPower wave energy converter has a rated capacity of 400 kW. To determine an appropriate new cut-off wave height, 30-year average capacity factors are calculated for different cut-off values to assess the impact of this reduction on the expected power production of the WEC. Table 2 indicates the 30-yr average capacity factors at France, Ireland, and Portugal for different cut-off wave heights.

$$CF = \frac{E_o}{P_o \cdot \Delta T} \tag{2}$$

	$CF_{H_s>10.5}$	$CF_{H_s>8}$	$CF_{H_s>7}$	$CF_{H_s>6}$
Capacity Factor France(%)	61.3	60.7	59.6	57.2
Capacity Factor Ireland(%)	52.1	51.8	51.2	49.8
Capacity Factor Portugal(%)	61.4	61.3	60.9	59.8

Table 2: Average 30-yr capacity factor for reduced power matrices in France, Ireland and Portugal.

Table 2 shows that lowering the PM cut-off wave height from 10.5m to 6m results in an annual loss of expected power production ranging from approximately 2% to 4%, depending on the location. This minor loss justifies the adjustment, as its significantly increases the likelihood of capturing at least one survival mode event per year. Additionally, the braking system of the WEC is protected in this way, as stopping the WEC from operation at 6 m instead of 10.5 m greatly reduces the forces induced on this system while only a small portion of expected power production is lost. Besides the PM reduction being necessary for the framework to be applicable across an increased number of sites, it may also extend the lifetime of the critical components of the braking system while maintaining acceptable power output.

3.1.3 Scatter Function

In order to determine E_0, the scatter function shown in Equation 3 is utilized. Here, $c_{i,j}$ represents the number of hours whose (H_s, T_e) pair falls into the bin defined by the i_{th} wave height interval and j_{th} energy period interval. N is the total number of valid hours in that year. In other words, $F(H_{s,i}, T_{e,j})$ represents how often that particular sea state occurs. For each location, the annual scatter function is determined and at a later stage it is multiplied with the PM to yield E_0.

$$F(H_{s_{i,j}} \cap T_{e_{i,j}}) \;=\; \frac{c_{i,j}}{N} \tag{3}$$

3.2 Computation and results

To compute E_0 for thirty years, a computational model is constructed. For each of the years a joint probability scatter function is computed which is multiplied with the PM and the timestep. Ultimately, E_0 for each

year from 1992 through 2021 is estimated. The individual steps of the computational model are detailed in Subsection 3.2.1, and the resulting outputs are presented in Subsection 3.2.2.

3.2.1 computational model

1. **Wave data extraction:** In this research, the ECHOWAVE hindcast dataset (Alday and Lavidas, 2024) is used. Via the Metocean-API (Metocean API Contributors, 2025) hourly time series of significant wave height H_s and peak frequency f_p are extracted for thirty years.

2. **Estimation of T_e:** The energy period is estimated with use of the calibration coefficient α, such that $T_e = \alpha T_p, \alpha = 0.90$. In Literature α is chosen based on spectral shape assumptions. This choice reflects a JONSWAP spectrum with $\gamma = 3.3$, representative of fetch-limited mid-Atlantic conditions. This estimations remains a widely used approximation for preliminary analyses. As Example, Table 3 shows a small slice of the 1995 time series for the first location. It includes all relevant variables needed to construct the scatter plots in step 4.

Date	Time	H_s (m)	$T_p = 1/f_p$ (s)	$T_e = 0.9 * T_p$ (s)
1995-01-01	00:00	4.602	13.33	11.99
1995-01-01	01:00	4.510	13.33	11.99
1995-01-01	02:00	4.398	13.16	11.84
⋮	⋮	⋮	⋮	⋮
1995-12-31	23:00	7.420	11.24	10.11

Table 3: Example of extracted hourly wave data for 1995 at Portugal.

3. **Scatter function:** For each of the 30 years of data, a two-dimensional histogram of (H_s, T_e) is constructed. To ensure direct compatibility with the PM, the histogram's bin edges for H_s and T_e are aligned with those of the PM. Specifically, H_s is divided into 29 bins of width 0.5 m and T_e is divided into 22 bins of width 1 sec. For each of the bins in the histogram the scatter function is defined as the fraction of hours spend in each bin, as shown in Equation 4. These fraction of hours spend at each bin must sum to one across all bins, which is stated in Equation 5.

$$F(H_{s_{i,j}} \cap T_{e_{i,j}}) = \frac{c_{i,j}}{N} \tag{4}$$

$$\sum_{i=1}^{29} \sum_{j=1}^{22} F(H_{s_{i,j}} \cap T_{e_{i,j}}) = 1 \tag{5}$$

4. **Scatter plots:** To illustrate the frequency of occurrence of each sea state, two representative scatter plot heatmaps are shown in Figure 5. Each heatmap shows the frequency of occurrence of each sea state pair (H_s, T_e) in the year 1996 and 1997. The horizontal axis shows T_e (0–21s in 1s steps), and the vertical axis shows H_s (0–14m in 0.5m steps). Darker red cells indicate higher frequency of occurrence (more hours spent in a sea state bin).

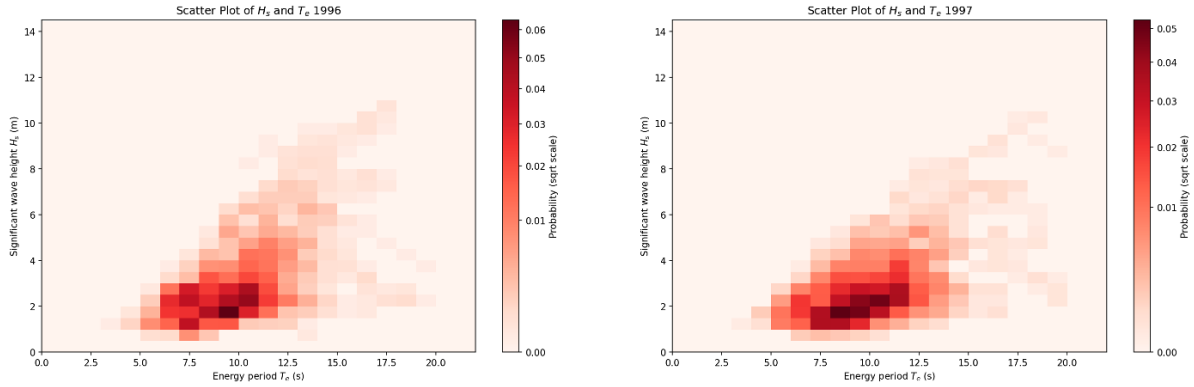

Figure 5: Scatter plots of the location in Portugal for the year 1996 and 1997

5. **Power production calculation:** Equation 6 shows how E_0 is computed. For each sea-state bin $(H_{s,i}, T_{e,j})$, the scatter function $F(H_{s,i}, T_{e,j})$ is multiplied by the corresponding $PM(H_{s,i}, T_{e,j})$, which represents the device's power output for that sea state. Summing these products over all 29×22 bins yields the device's long term average power. Multiplying that average by the total operating time $\Delta t = 24hr * N$ (where N is the number of operational days in a year) gives E_0. Repeating this calculation for each year from 1992 to 2021 produces thirty values of E_0.

$$E_{\text{year}} = \sum_{i=1}^{29} \sum_{j=1}^{22} \Big[F(H_{s_{i,j}} \cap T_{e_{i,j}}) \times PM(H_{s,i}, T_{e,j}) \Big] \times \Delta T, \tag{6}$$

3.2.2 Results

The E_0 and CF for France are shown in Table 4 as an example, the results for all three locations are shown in Appendix A.1. The capacity factor (see Equation 2) is included as a sanity check for the annual power production calculation.

Year	E_0 (MWh)	CF (%)	**Year**	E_0 (MWh)	CF (%)	**Year**	E_0 (MWh)	CF (%)
1992	2266.6	64.5	**2002**	2149.3	61.3	**2012**	2057.4	58.6
1993	2018.8	57.6	**2003**	1963.2	56.0	**2013**	2055.6	58.7
1994	1992.4	56.9	**2004**	1950.9	55.5	**2014**	1930.0	55.1
1995	1862.7	53.2	**2005**	1877.5	53.6	**2015**	2215.0	63.2
1996	1944.5	55.3	**2006**	1931.9	55.1	**2016**	2047.8	58.3
1997	1928.2	55.0	**2007**	1807.6	51.6	**2017**	1960.7	56.0
1998	1967.8	56.2	**2008**	2174.3	61.9	**2018**	2120.3	60.5
1999	2052.7	58.6	**2009**	1965.6	56.1	**2019**	2016.3	57.5
2000	2010.0	57.2	**2010**	1866.5	53.3	**2020**	2017.1	57.4
2001	1917.9	54.7	**2011**	2209.9	63.1	**2021**	1919.4	54.8

Table 4: Annual power production and CF for France

4 Load Model

As indicated in Figure 6, this section focuses on computing the annual peak heave loads F_p on the Corpower C4 inspired WEC. A Python script is constructed that combines Capytaine Boundary Element Method (BEM) (Ancellin and Dias, 2019; Babarit and Delhommeau, 2015) outputs with Morison's drag and inertia terms. This hybrid approach yields the maximum heave load on the converter for each annual extreme sea state. This section begins with a description of the modeling approach for the WEC under extreme scenarios (see Subsection 4.1), followed by the annual extreme sea states used as input (see Subsection 4.2), and concludes with the methodology (see Subsection 4.3) and the computational steps and results (see Subsection 4.4).

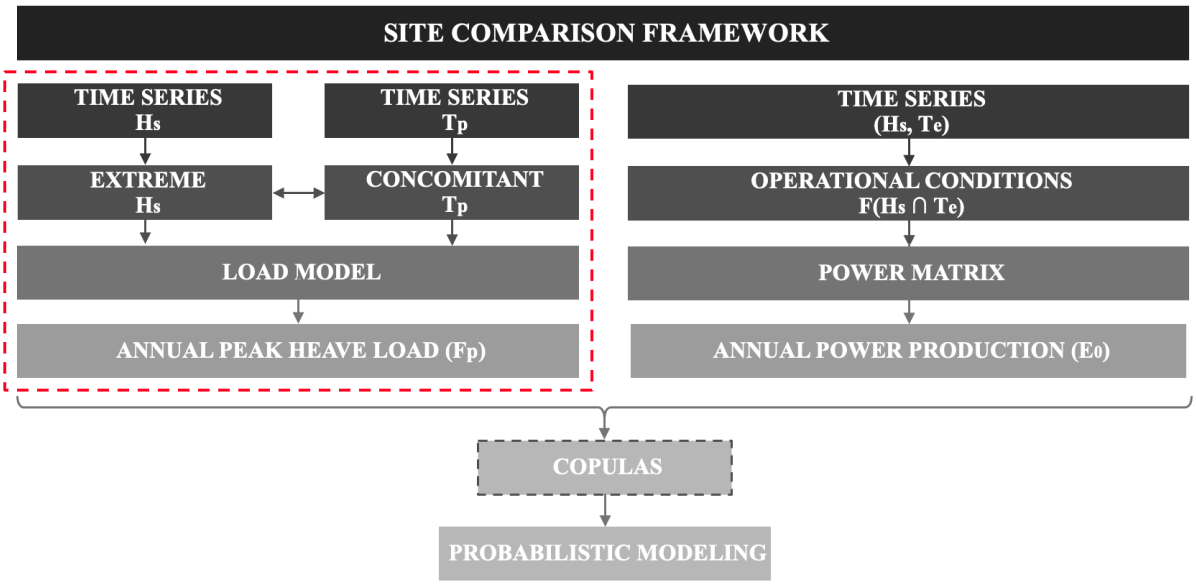

Figure 6: Copula-based site comparison framework, Section 4 focuses on the left-hand "Load Model" branch (in red) which feeds F_p into the copula model.

4.1 Modeling Approach

The load model branch in Figure 6 computes F_p on the WEC when it is in survival mode. In the Corpower-C4 inspired design, "survival mode" means the significant wave height H_s exceeds 10.5 m. At that point, the device locks out all PTO motion and the entire body remains fixed in the water, protecting the PTO. The body is held stationary until conditions ease and H_s falls below the threshold again. For these extreme conditions, when the device is in survival mode, the heave loads that the braking system must endure are calculated. Figure 7 shows the simplified modeling scenario: a vertical cylinder of diameter D and draft d with the same mass and dimensions as the C4 device, placed in an infinite-depth ocean ($h = \infty$). A regular wave with crest amplitude a and wavelength λ travels in positive x direction. Under these fixed-body, deep-water, regular-incoming-wave assumptions, F_p is calculated.

By using a regular incoming wave with a single frequency ω and amplitude a, it ensures that when the Capytaine BEM solver (Ancellin and Dias, 2019; Babarit and Delhommeau, 2015) uses this as input it returns hydrodynamic coefficients and an excitation force amplitude for that single frequency ω. If an irregular sea state was used as input (a spectrum of many frequencies ω_i), the BEM solver would give coefficients and amplitudes for each of the frequencies ω_i embedded in the irregular sea state. Copula can only model dependencies between scalar values. Therefore, all those frequency specific results would then

have to collapse into a single extreme force via spectral integration, which is computationally intensive. Because this study is focuses on comparing sites rather than designing a device, a single frequency regular wave provides a consistent and computationally efficient approach for estimating F_p across different locations.

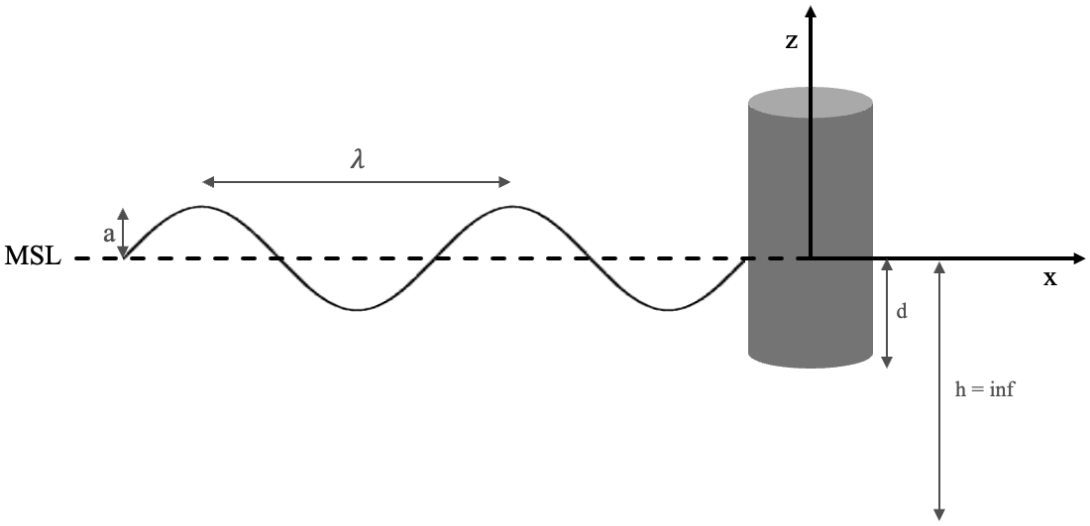

Figure 7: Modeling approach

4.2 Extreme Sea States

From the ECHOWAVE data set, the highest occurred annual significant wave heights H_s and their concomitant wave period T_p are selected. Table 5 presents the extreme sea states for France as an example, while the extreme sea state data for all other locations is shown in Appendix B.1. For each of these sea states, a F_p is calculated. The methodology used for this calculation is discussed in the following Subsection 4.3.

Year	$H_s(m)$	$T_p(s)$	**Year**	$H_s(m)$	$T_p(s)$	**Year**	$H_s(m)$	$T_p(s)$
1992	8.33	17.86	**2002**	11.06	19.61	**2012**	9.86	16.39
1993	10.02	17.86	**2003**	9.15	20.83	**2013**	9.66	12.66
1994	13.75	17.86	**2004**	10.48	14.29	**2014**	16.77	18.87
1995	11.39	13.89	**2005**	10.57	13.70	**2015**	10.19	16.95
1996	11.40	18.18	**2006**	9.66	16.67	**2016**	13.42	21.28
1997	10.01	13.70	**2007**	14.32	18.18	**2017**	13.23	18.87
1998	12.18	16.67	**2008**	14.75	19.23	**2018**	10.37	17.86
1999	10.50	12.82	**2009**	10.10	16.39	**2019**	10.17	20.00
2000	9.67	13.89	**2010**	11.72	17.86	**2020**	11.51	16.13
2001	9.15	17.86	**2011**	10.53	21.74	**2021**	11.33	17.54

Table 5: Annual maximum significant wave height and concomitant peak period France

4.3 Methodology

This subsection outlines the methodologies used for computing F_p on the WEC by proceeding through three steps: first, defining the device geometry and surface mesh, second, applying a Boundary Element Model (BEM) to compute frequency dependent hydrodynamic coefficients and wave excitation amplitude, and third, using Morison's equation to evaluate inertial and drag contributions.

4.3.1 Geometry and Mesh Size

The body used for the load model is simplified and modeled as a cylinder with diameter $D = 9m$, draft $d = 6m$ and height $H = 12m$. The mean sea level is set at $z = 0$, and the cylinder's axis lies at $x = 0$, $y = 0$. The device mass is $70000kg$. Figure 8 depicts the body and its defining geometries.

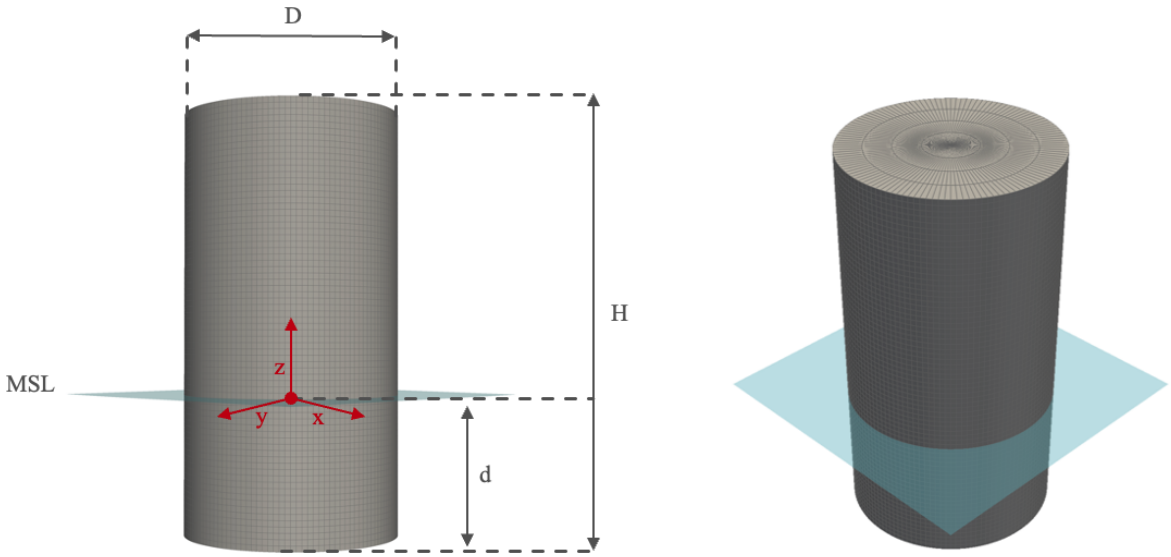

Figure 8: Simulation model of body

To select an appropriate surface discretization, a mesh convergence study was conducted in Capytaine (Ancellin and Dias, 2019; Babarit and Delhommeau, 2015). Each mesh is defined by (n_f, n_c, n_v), where n_f denotes panels on each circular face, n_c panels around the circumference, and n_v panels along the height. The mesh (n_f, n_c, n_v) is refined until the heave-added-mass coefficient A_{33} changed by less than 1%. Table 6 shows that for a meshing of $(6, 192, 108)$ the added mass converges to $210.0 * 10^3 kg$. This mesh size will be used for all subsequent F_p calculations.

mesh size (n_f, n_c, n_v)	(2, 16, 9)	(4, 64, 36)	(4, 128, 72)	(6, 192, 108)	(8, 256, 144)
added mass A_{33} (10^3 kg)	215.5	212.0	209.9	210.0	210.4
relative change (%)	—	1.6%	1.0 %	0.05%	0.2%

Table 6: Mesh convergence for added mass coefficient A_{33}.

4.3.2 Boundary Element Method

The boundary element method is a fast, automated way to obtain frequency-dependent hydrodynamic coefficients for the body defined in 4.3.1. The linear potential flow BEM solver solves a surface integral equation for the fluid potential under both radiation and diffraction boundary conditions. The model returns the added mass, radiation coefficients, and excitation force amplitude. For the modeling approach in this research, only the added mass and excitation amplitude are extracted and used from the BEM solver; for further reasoning on this, see Subsection 4.4.1, where all steps to determine the extreme heave load are explained.

4.3.3 Morison's Equation

Morison's equation 7 is used to compute the hydrodynamic load on a slender body when the dimension is small compared to the wave length. The equations takes viscous drag and inertia into account and it assumes the incident wave is not effected by the presence of the device due to its small dimension (Subbulakshmi et al., 2022).

$$F(t) = \underbrace{\rho\, C_m\, V\, \dot{U}(t)}_{\text{inertia / added-mass}} + \underbrace{\frac{1}{2}\,\rho\, C_d\, A\, \big|U(t)\big|\, U(t)}_{\text{drag}} \tag{7}$$

where:

- ρ is the fluid density,
- C_m is the added-mass coefficient,
- V is the displaced volume (or per-unit-length area),
- C_d is the drag coefficient,
- A is the reference area,
- $U(t)$ is the fluid velocity relative to the body.

4.4 Computation and Results

The load model computes F_p on the fixed body. These F_p values are referred to as the extra load on top of the equilibrium state induced by the incoming regular extreme wave. The model assumes that at the equilibrium position, any imbalance between the buoyant force and the structure's weight is compensated by the pre-tensioning system. When the wave crest arrives, the model only considers the extra forces on top of the equilibrium state. Because in equilibrium position $F_{weight} + F_{bouyancy} + F_{mooring} = 0$, they are ignored in the model. Under this assumption and with the body held in a fixed position. radiation damping and PTO forces vanish. Therefore, F_p reduces to Equation 8. Here F_{exc} is the wave excitation force, F_{drag} and $F_{inertia}$ are the Morison drag and inertia terms in Equation 7.

$$F_p = \underbrace{F_{exc}}_{\text{BEM}} + \underbrace{F_{drag} + F_{inertia}}_{\text{Morison's}} \tag{8}$$

A computational model is constructed to compute F_p each extreme sea state shown in Appendix B.1. The following Subsection 4.4.1 discusses its specific steps.

4.4.1 Computational Model

To compute F_p, a computational model consisting of several steps is constructed. This subsection outlines those steps and their corresponding justification. The core of the model utilzies the Capytaine BEM solver (Ancellin and Dias, 2019; Babarit and Delhommeau, 2015) to solve the linear potential flow diffraction problem, providing the complex wave excitation amplitude added mass in heave direction.

1. **Geometry and Mesh:** A vertical cylinder mesh with associated diameter, length and draft is defined. The cylinder is positioned in its equilibrium position by setting the bottom at $z = -draft$ and its top at $z = -draft + length$. The geometric midpoint of the cylinder lies at $z = \frac{length}{2} - draft$ relative to the mean sea level ($z = 0$).

2. **Wave Parameters:** In this simplified model a regular wave with a single frequency ω and wave height H_s is used as an input. Although BEM can be run over a range of wave frequencies ω to build a full excitation spectrum, in this research the copula based analysis requires only a single scalar value for F_p for each of the extreme sea states. By selecting a single frequency as input, one wave excitation amplitude and one added-mass value for that specific frequency ω can be obtained.

3. **BEM Solver:** A floating body object is created by combining the surface mesh with its degrees of freedom, here only a single heave DOF is assigned. Capytaine (Ancellin and Dias, 2019; Babarit and Delhommeau, 2015) then computes and returns the frequency-dependent hydrodynamic coefficients: added mass A_{33}, radiation damping B_{33}, diffraction force, Froude-Krilov force and total excitation force. For the survival mode scenario only the added mass and the excitation force influence the extra hydrodynamic load on the fixed structure under a passing wave. These contributors can be described and derived as follows:

    - **Wave Excitation Force:** The wave excitation force consists of the Froude-Krilov and diffraction force. The Froude-Krylov force represents the pressure on the body from the undisturbed incident wave. the pressure is derived from the the velocity potential of the wave, it is integrated over wetted surface of the body which gives the Froude-Krylov force. The diffraction force is the wave pressure resulting from waves diffracting off the surface of the hull, the pressure is found by solving the linear diffraction problem and integrating those diffracted wave pressures over the wetted surface (Alves, 2016). For the frequency ω of a regular incoming extreme wave, the BEM solver combines the diffraction and Froude-Krylov force and returns a single complex excitation force amplitude $\widehat{F}_{\text{exc}}(\omega)$ for a frequency ω in heave direction.
    - **Added Mass:** The added mass A_{33} represents the effective mass of fluid that "sticks" to the cylinder when it moves in the vertical direction. In the BEM solver, this coefficient is obtained by prescribing a unit heave oscillation of the body and integrating the resulting pressure field to find the inertia force, giving A_{33} as the heave-heave added mass. In the survival mode the cylinder itself is fixed, but the water still accelerates vertically under the passing wave. Therefore A_{33} is used to convert that fluid acceleration into the inertia force on the stationary structure defined with Equation 9. Here $\dot{u}(t)$ is the fluid acceleration and $A_{33}(\omega)$ is the added mass for the frequency ω of a regular incoming extreme wave.

$$F_{\text{inertia}}(t) \;=\; A_{33}(\omega)\,\dot{u}(t) \tag{9}$$

4. **Wave Kinematics:** To compute inertial and drag forces, a deep water regular wave is assumed. Under these conditions the fluid motion can be defined by Airy's linear wave theory (Airy, 1841). For a regular wave characterized by amplitude a, angular frequency ω, and wave number k. The velocity potential can be described with Equation 10. The vertical and orbital velocity can then be described with equation 11 and 12 (Krogstad and Arntsen, 2010).

$$\phi(x,z,t) = \frac{a\,g}{\omega}\,e^{kz}\,\sin\big(kx-\omega t\big), \tag{10}$$

$$u(x,z,t) = \frac{\partial \phi}{\partial z} = a\,\omega\,e^{kz}\,\sin\big(kx-\omega t\big) \tag{11}$$

$$\dot{u}(x,z,t) \;= \frac{\partial u}{\partial t} = -\,a\,\omega^2\,e^{kz}\,\cos\big(kx-\omega t\big) \tag{12}$$

5. **Peak Heave Load Computation:** The wave excitation term in Equation 8 dominates F_p. Therefore, the peak load occurs when the wave crest passes directly over the cylinder, maximizing the wave excitation force. At that instant, the inertia and drag terms in Morison's equation (dependent on orbital velocity and acceleration) must be evaluated. Under the assumptions of deep water and regular waves, the surface elevation is given by Equation 13, where $k = \frac{\omega^2}{g}$.

$$\eta(x,t) = a\,\cos\big(kx - \omega t\big) \tag{13}$$

The surface elevation reaches its peak when $\cos\big(kx - \omega t\big) = 1$. Then the velocity $u(x,z,t) = 0$ (drag vanishes) and acceleration $\dot{u}(x,z,t) = -\,a\,\omega^2\,e^{kz}$. With these kinematics defined for the instant where the wave crest passes directly over the cylinder, the final expression for the maximum heave load is described with Equation 14. Because $\lambda_{wave} << D$, the fluid acceleration is uniform along the draft so a single value for the acceleration is used to compute the inertia force. The BEM solver returns a complex excitation force amplitude $\widehat{F}_{\text{exc}}$. To obtain its peak magnitude, the absolute value $|\widehat{F}_{\text{exc}}|$ is taken. Finally, because $|\widehat{F}_{\text{exc}}(\omega)|$ is given per meter of wave elevation, multiplying by the maximum crest amplitude a yields the maximum excitation force.

$$F_p = \underbrace{\big|\widehat{F}_{\text{exc}}\big| * \frac{H_{max}}{2}}_{\text{Excitation Force}} + \underbrace{A_{33}(\omega) * a\,\omega^2\,e^{kz}}_{\text{Inertia Force}} \tag{14}$$

4.4.2 Results

The load model uses the extreme sea states as input to estimate the associated F_p on the Corpower C4 inspired wave energy converter. Table 7 depicts the extreme sea states and the associated F_p for France, the results for the other locations are shown in Appendix B.2.

Year	$H_s(m)$	$T_p(s)$	$F_p(kN)$	**Year**	$H_s(m)$	$T_p(s)$	$F_p(kN)$	**Year**	$H_s(m)$	$T_p(s)$	$F_p(kN)$
1992	8.33	17.86	2265	**2002**	11.06	19.61	3093	**2012**	9.86	16.39	2599
1993	10.02	16.39	2641	**2003**	9.15	20.83	2599	**2013**	9.66	12.66	2226
1994	13.75	17.86	3738	**2004**	10.48	14.29	2595	**2014**	16.77	18.87	4639
1995	11.39	13.89	2778	**2005**	10.57	13.70	2558	**2015**	10.19	16.95	2720
1996	11.4	18.18	3118	**2006**	9.66	16.67	2563	**2016**	13.42	21.28	3831
1997	10.01	13.70	2422	**2007**	14.32	18.18	3916	**2017**	13.23	18.87	3660
1998	12.18	16.67	3231	**2008**	14.75	19.23	4103	**2018**	10.37	17.86	2820
1999	10.5	12.82	2440	**2009**	10.10	16.39	2662	**2019**	10.17	20.00	2859
2000	9.67	13.89	2358	**2010**	11.72	17.86	3187	**2020**	11.51	16.13	3014
2001	9.15	17.86	2488	**2011**	10.53	21.74	3021	**2021**	11.33	17.54	3062

Table 7: Extreme sea states and the associated F_p for France

5 Probabilistic Modeling

In the previous Sections 3 and 4, the computations and results of the annual power production E_0 and peak heave load F_p pairs at three different sites are presented. This section focuses on modeling the dependency between the two variables for each of the sites using copulas. Subsection 5.1 describes the marginal fitting process, while Subsection 5.2 outlines the data preparation required for fitting a copula in Subsection 5.3. The results are later used in Section 6 to assess trade-offs between sites, possibly impacting site suitability. Throughout this section example plots are provided only for Ireland, the plots for France and Portugal are presented in the Appendix.

5.1 Marginal Parametric Distribution Fitting

In order to infer values of the random variables with unseen probabilities within the observations, parametric marginals for E_0 and F_p are determined. This is essential because the copula must assess values beyond historical observations. Relying on an empirical distribution would restrict all simulated pairs to the past range. Parametric fits enable the estimation of extreme scenarios that have not been observed within the available historical data. This subsection covers the selection and fitting of the parametric distributions. First, empirical histograms for each margin are constructed. Then, candidate distributions are selected by visual inspection. Finally, each candidate is fitted via maximum loglikelihood and the best model is chosen using goodness-of-fit tests. These tests consist of (i) the visual fit to log-scale exceedance plots, (ii) examination of QQ-plots, and (iii) the Kolmogorov–Smirnov (KS) test.

5.1.1 Candidate Distributions

For each location E_0 and F_p are binned into density histograms. For each bin i, containing k_i of the n observations and having width Δx, the bin height is calculated as:

$$f_i = \frac{k_i}{n\,\Delta x}. \tag{15}$$

These histograms reveals a indication of the skewness and tail behavior of each margin. Based on those visual cues, candidate distributions are selected for each variable (Wilks, 2011) and then fitted by maximum loglikelihood estimation. Below is an example for Ireland, where the motivation for the selection of each candidate distribution is discussed and the fitted distributions are shown. The motivation and fits for all locations can be found in Appendix C. The analytical expressions for each of these fitted distributions are provided in Appendix F.

- **Candidate distribution selection example Ireland:** The F_p histogram shown on the left in Figure 9, peaks near 2600–2800 kN and seems to show a light negative skew towards 3400 kN. Gamma and Log-Normal address a light postive skew, the Normal provides a symmetric baseline, and GEV and GumbelMin model a fatter lower tail. The E_0 histogram, shown on the right in Figure 9, centers around 1700–1800 MWh and exhibits a light negative skew. To model the moderate asymmetry, Normal, Gamma, and Log-Normal fits are applied, while GumbelMin captures the slightly heavier left tail.

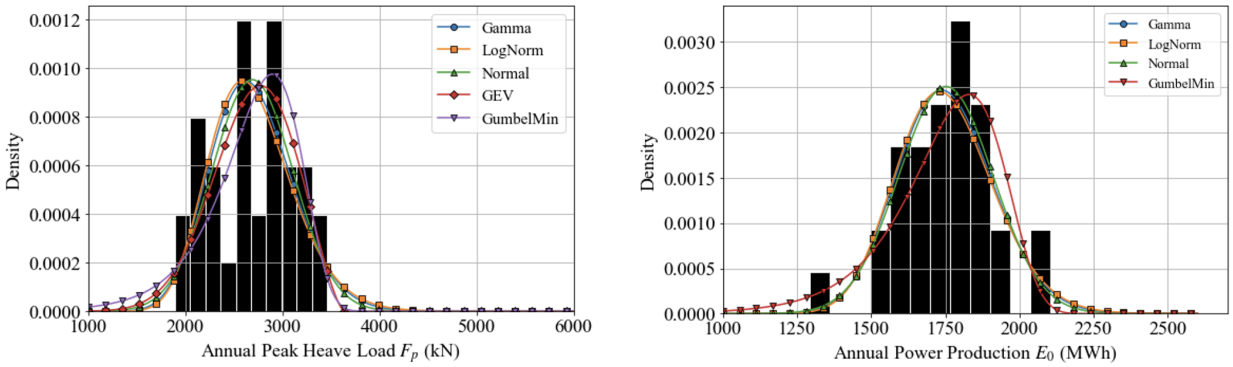

Figure 9: E_0 (right) and F_p (left) histograms and fitted parametric distributions for Ireland

5.1.2 Goodness-of-Fit Assessment

From the candidate distributions, the best fitting distribution must be selected for each variable at each location. To assess how well each distribution fits the data, (i) the visual fit to the log-scale exceedance plots is checked, (ii) QQ-plots are examined, and (iii) Kolmogorov–Smirnov tests are applied. QQ-plots indicate how closely predictions of a variable match the actual value. Based on how closely the predicted values follow the 45° line it can be determined visually which distribution is the best model. The Kolmogorov–Smirnov test provides a numerical measure of fit by quantifying roughly the maximum vertical distance D_n between the empirical CDF $F_n(x)$ and fitted parametric CDF $F_\theta(x)$ as indicated in Equation 16. Here $\sup_x$ is the supremum of the set of distances, which can be interpreted as the largest absolute difference between the two distribution functions across all values of the random variable X. Once D_n is computed, the associated p-value is obtained under the null hypothesis that the sample comes from F_θ. A large p-value indicates that an observed discrepancy of size D_n is plausible by chance, whereas a small p-value leads to rejection of the fitted model.

$$D_n = \sup_x \left| F_n(x) - F_\theta(x) \right| \tag{16}$$

The goodness-of-fit process for the E_0 and F_p distributions of Ireland is presented below as an example. The goodness-of-fit measures for Portugal and France are analyzed in a similar manner but are not discussed in detail in this Subsection. The results of the goodness-of-fit measures for all locations are shown in Appendix D.

- **Goodness-of-fit example Ireland:** Figure 10 depicts the QQ-plot (bottom row) and the log-scale exceedance plots (top row) for E_0 (left column) and F_p (right column). The log-scale exceedance plots shows that the fitted Gamma, LogNorm, and Normal distributions best fit the empirical data, while GumbelMin underestimates the upper tail of E_0. For F_p, Gamma, LogNormal, and Normal are also reasonable fits, while GEV and GumbelMin underestimate the upper tail. The QQ-plots indicate that the Normal distribution best represents the empirical data for E_0, while F_p, multiple distributions show similar results. The KS test shows that for the Normal distribution fitted to E_0, the p-value is highest and D_n is smallest compared to the other candidates. Based on results of the KS values, QQ-plot, and the log-scale exceedance plots, the Normal distribution is chosen as most suitable fit for E_0 in Ireland. For F_p the most suitable distributions based on the KS test are the Normal, GEV, and GumbelMin distributions. However, since GumbelMin and GEV tend to underestimate the upper tail of the peak heave load, these two are excluded, and the Normal distribution is chosen as the most suitable fit for the F_p distribution in Ireland.

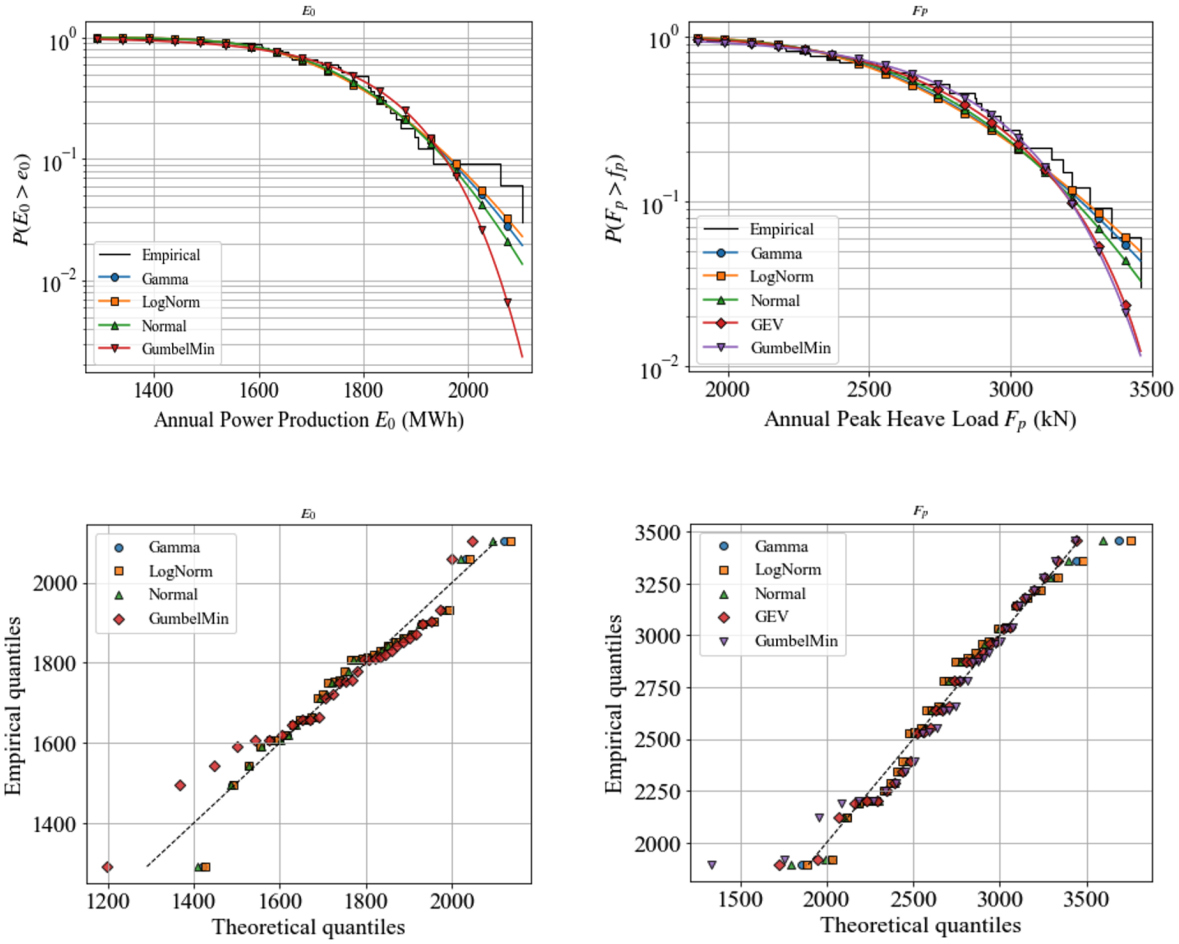

Figure 10: log-scale exceedance plots (top row) and QQ plots (bottom row) for E_0 (left column) and F_P (right column)

Table 8 summarizes the chosen distribution by location and variable, along with its KS p-value. Each margins best fitting distribution is chosen as in the Ireland example where (i) D_n and p-value are compared, (ii) QQ-plots are analyzed, and (iii) the visual fit to log-scale exceedance plots is checked.

Location	**Variable**	**Distribution**	p**-value**	**Parameter**	**Notation**	**Value**
France	E_0	GumbelMax (μ_{GM}, β_{GM})	0.95	Location	μ_{GM}	1954.89
				Scale	β_{GM}	91.51
France	F_p	GumbelMax (μ_{GM}, β_{GM})	0.81	Location	μ_{GM}	2715.34
				Scale	β_{GM}	414.47
Portugal	E_0	GEV $(\xi_{GEV}, \mu_{GEV}, \sigma_{GEV})$	0.99	Shape	ξ_{GEV}	0.4368
				Location	μ_{GEV}	2070.20
				Scale	σ_{GEV}	104.18
Portugal	F_p	Normal (σ_N, μ_N)	0.68	Mean	μ_N	2462.78
				Standard deviation	σ_N	545.84
Ireland	E_0	Normal (σ_N, μ_N)	0.83	Mean	μ_N	1751.99
				Standard deviation	σ_N	159.08
Ireland	F_P	Normal (σ_N, μ_N)	0.82	Mean	μ_N	2691.98
				Standard deviation	σ_N	418.35

Table 8: Fitted parametric distributions

5.2 Data Preparation

In order to fit a copula the data must be prepared. This is done because copulas can only operate on variables whose marginal distributions have been mapped to uniform scale [0,1]. This standardization removes differences in units, scale, and distribution shape, leaving only the pure dependence structure between the variables. This subsection first lays the foundation before mapping the data to uniform space. This foundation consists of defining the variable notation and presenting the raw data in their original units, scales and marginal distributions. Once this background has been established, each of the annual observations (E_0, F_p) is transformed to uniform scale using a empirical CDF (ECDF).

5.2.1 Raw Data

Figure 11 shows the joint behavior of E_0 and F_p in their original space for Ireland. The top-left and bottom-right figures show each of the margin histograms fitted with its parametric distribution. The top-right and bottom-left figures present the scatterplots (E_0, F_P) and (F_P, E_0) respectively. Each pair represents one of the years from 1992 until 2021 yielding thirty data points in total.

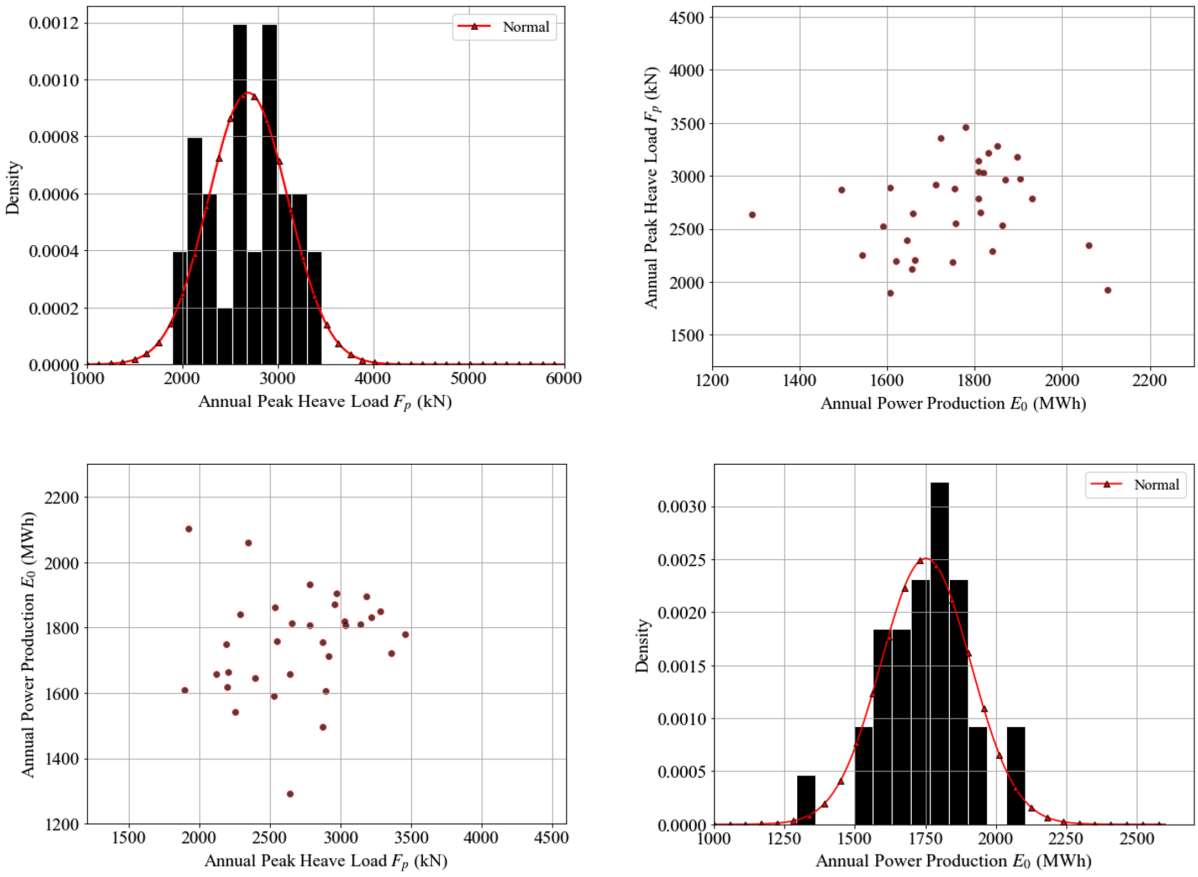

Figure 11: Scatter matrix of untransformed (E_0, F_p) pairs for Ireland

5.2.2 Variable Definition

For the remaining of this section the following notation holds for the annual power production E_0 and maximum heave load F_p in year i (with $i = 1$ for 1992 and $i = 30$ for 2021):

$$X_i = E_{0,i}, \qquad Y_i = F_{p,i}$$

5.2.3 Empirical Cumulative Distribution Function

Before a copula can be fitted, the marginals in the scatter matrix shown in Figure 11 must be converted to uniform scale to isolate the dependence. Instead of imposing a specific parametric form, which might result in modeling mismatches, the empirical cumulative distribution function (ECDF) is calculated. Equations 17 and 18 define the ECDF of the samples $X_1, \ldots, X_n$ and $Y_1, \ldots, Y_n$. Evaluating these functions at the observed data points (X_i, Y_i) yields rank-based pseudo-observations, depicted in Equation 19. These lie in a set of $1/n, 2/n \ldots, 1$ with a sample size $n = 30$.

$$\hat{F}_X(x) = \frac{1}{n+1} \sum_{i=1}^{n} \{X_i \leq x\}, \tag{17}$$

$$\hat{F}_Y(y) = \frac{1}{n+1} \sum_{i=1}^{n} \{Y_i \leq y\} \tag{18}$$

$$u_i = \hat{F}_X(x), \quad v_i = \hat{F}_Y(y), \qquad i = 1, \ldots, n. \tag{19}$$

For Ireland, Figure 12 presents the scatter plot with margins in original units (left plot), and the rank-based pseudo-observation scatter plot with uniform margins (right plot). Here each observation (u_i, v_i) is obtained by applying the ECDF to the annual power production $E_{0,i}$ and peak heave load $F_{h,i}$, mapping them into the unit interval $[0, 1]$ via Equation 17 and 18.

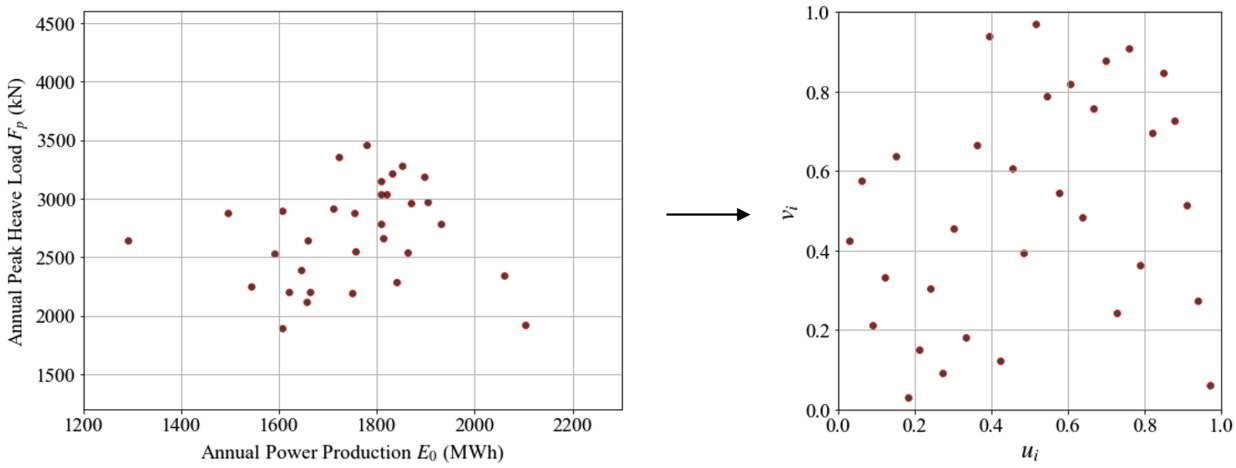

Figure 12: Ireland example transformation of marginals from original to uniform space

5.3 Copula Fitting

Five candidate copula families are fitted to the (u_i, v_i) pairs for each of the three locations. For each family, the dependence parameters are estimated via maximum loglikelihood estimator (see Section 5.3.1), and the quality of fit is assessed via Cramér–von Mises, Akaike Information Criterion, and quadrant semi-correlations (see Section 5.3.2). By comparing these goodness-of-fit measures, the copula family that best captures the joint dependence at each location is selected (see Section 5.3.3). The five copulas families to be

fitted are shown in Figure 13. These families consist of both archimedian and elliptical families that should capture most bivariate dependence patterns. Fitting these five families covers models with and without tail dependence.

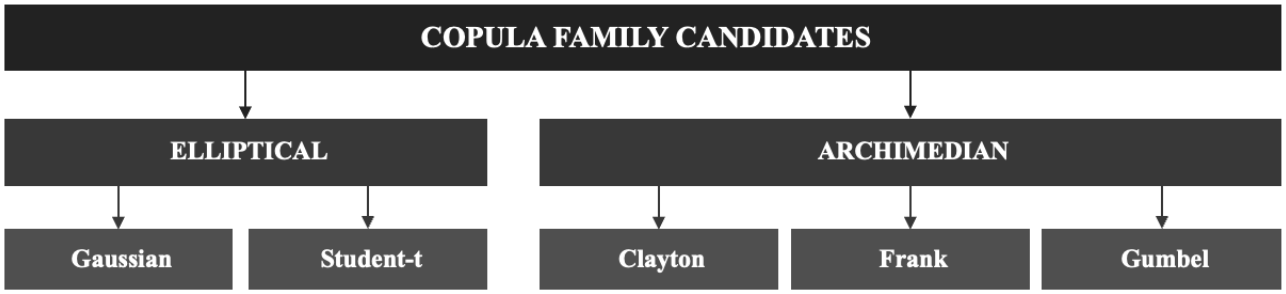

Figure 13: Copula family candidates

5.3.1 Fitting Copula Parameters

Pyvinecopulib (pyvinecopulib, 2019) is an open source Python package developed for the use of bivariate copulas and vine-copulas. One of the functions in this package automatically fits and selects the most suitable bivariate copula family based on Akaike Information Criterion. Utilizing this package will be the starting point, yielding a library of candidate bivariate copula models with their associated parameters. Pyvinecopulib uses the pseudo observations $(u_i,\ v_i)$ as input (see Subsection 5.2.3) and returns the fitted parameters of the candidate copula families, these results are shown in Table 9. The first and second columns indicate the copula family and its parameter notation respectively. The remaining columns report the values of each copula parameter for the five copula families and three locations. A goodness-of-fit assessment is utilized in Subsection 5.3.2, where the most suitable copula model for each location from Table 9 is selected.

Copula Family	**Parameters**	**France**	**Portugal**	**Ireland**
Gaussian	$C_{\text{ga}}(u, v; \rho_{ga})$	$C_{\text{ga}}(u, v; -0.21)$	$C_{\text{ga}}(u, v; -0.42)$	$C_{\text{ga}}(u, v; 0.24)$
Student-t	$C_{st}(u, v; \rho_{st}, \nu_{st})$	$C_{st}(u, v; -0.11, 4.00)$	$C_{st}(u, v; -0.41, 50)$	$C_{st}(u, v; 0.28, 8.70)$
Clayton	$C_{\text{cl}}(u, v; \theta_{cl})$	$C_{\text{cl}}(u, v; 1.8 \cdot 10^{-6})$	$C_{\text{cl}}(u, v; 1.8 \cdot 10^{-6})$	$C_{\text{cl}}(u, v; 0.42)$
Frank	$C_{\text{fr}}(u, v; \theta_{fr})$	$C_{\text{fr}}(u, v; -0.67)$	$C_{\text{fr}}(u, v; -2.20)$	$C_{\text{fr}}(u, v; 1.80)$
Gumbel	$C_{\text{gu}}(u, v; \theta_{gu})$	$C_{\text{gu}}(u, v; 1.00)$	$C_{\text{gu}}(u, v; 1.00)$	$C_{\text{gu}}(u, v; 1.20)$

Table 9: Fitted copula families

5.3.2 Goodness-of-Fit Assessment

The five fitted copula families are compared for each location to identify the model that best captures the observed joint behavior. In this subsection, three goodness-of-fit measures are utilized: (i) the Cramér–von Mises statistic, (ii) Akaike Information Criterion (AIC) and (iii) the quadrant semi-correlations. Each method is briefly described, followed by the corresponding results.

1. **Cramer Von Misses** is goodness-of-fit measure that uses the empirical copula $C_n(u, v)$ as a benchmark, shown in Equation 20. The empirical copula is constructed from the data's pseudo-observations, it

describes the proportion of observations falling in rectangle [0,u] and [0,v]. The empirical copula serves as a nonparametric benchmark for the Cramér–von Mises (CvM) goodness-of-fit measure, which assesses how closely the fitted parametric copula $C_\theta(u, v)$ models the observed dependence structure. Equation 21 shows the CvM statistic S_n, for the sample (u_i, v_i). A smaller S_n indicates that the parametric copula closely follows the empirical copula, whereas a larger S_n signals a poorer overall fit. However, S_n alone does not reveal which regions of the unit square (tail or near center) contribute most to the discrepancies.

$$C_n(u, v) \;=\; \frac{1}{n+1} \sum_{i=1}^{n} \mathbf{1}\{\, u_i \le u,\; v_i \le v\} \tag{20}$$

$$S_n = \; n \sum_{i=1}^{n} \big[C_n(u_i, v_i) \;-\; C_\theta(u_i, v_i)\big]^2. \tag{21}$$

2. **Akaike Information Criterion (AIC)** (Akaike, 1973) is a model selection measure, shown in Equation 22. Here k is the number of estimated parameters in the model and $\widehat{L}$ is the maximized likelihood. The information criterion combines the maximum log-likelihood with penalizing the number of parameters involved, balancing fit against complexity. The model with the lowest AIC is expected to best approximate the observed data.

$$\text{AIC} \;=\; 2\,k \;-\; 2\ln\big(\widehat{L}\big) \tag{22}$$

3. **Quadrant semi-correlation** assesses the correlation between two variables within each region of their joint distribution. Within each quadrant only the data in that region is used to compute the Pearson's correlation coefficient ρ between U and V shown in Equation 24. Here U and V are the standard normal transforms of the original pseudo observations u and v defined by Equation 23. The pseudo observations are mapped to standard normal space to create a symmetric distribution centered at zero. This plane is divided into four quadrants: NE (high-high), NW (low-high), SW (low-low), and SE (high-low). For each quadrant, the correlation coefficient ρ is calculated on the transformed observed data and then on samples simulated from each of the five candidate copula families. By comparing these quadrant semi-correlations it can be determined which copula family most closely matches the dependence structure of the observed data.

$$U = \Phi^{-1}(u) \quad \text{and} \quad V = \Phi^{-1}(v) \tag{23}$$

$$\rho \;=\; \frac{\mathrm{Cov}(U,\, V)}{\sigma_U\, \sigma_V} \tag{24}$$

The semi-correlation values for Portugal are shown in Figure 28 in Appendix E.4. The results from the empirical data (30 pseudo-observations) differ significantly from those derived from simulated samples of the fitted parametric copulas. The small sample size could cause overestimation or instability in these quadrant correlations and lead to a mismatch with the simulated values. Therefore, in this research the semi-correlation values will no longer be used for copula model comparison. However the quadrant semi-correlations derived from the observed data do indicate that there is no significant tail dependence, hinting that models such as Frank and Gaussian could be a suitable option.

4. **Spearman's rank correlation coefficient** r (Spearman, 1904) is a non-parametric measure of the strength and direction of a monotonic relationship between two variables, as shown in Equation 25. Here u and v are the normalized ranks of the two variables. $\mathrm{Cov}(u, v)$ denotes the covariance between u and v and σ_u and σ_v represent their standard deviations.

$$r = \frac{\mathrm{Cov}(u, v)}{\sigma_u\, \sigma_v} \tag{25}$$

The value for r ranges from -1 to $+1$, where $+1$ or -1 imply an exact positive or negative monotonic relationship and 0 no correlation. The p-value indicates the likelihood that uncorrelated variables produce a r at least as extreme as the one computed from the data set. This p-value indicates whether a statistically significant dependency exists between the variables at each site. A significance level of $\alpha = 0.15$ is chosen as a threshold for declaring a dependency between variables statistically significant. This relatively high threshold is justified by the nature of the study and the limitations of the data. The datasets used have a relatively small sample size of n=30, which limits the statistical significance and increases the risk of failing to detect true dependencies. This could result in high p-values even when dependence is present. Since the study focuses on copula utilization, missing dependency and therefore not modeling a copula hinders meaningful comparison of results and limits the ability to assess the capabilities of the framework. On the other hand, incorrectly assuming dependence and modeling a copula where there is none carries little consequence to the goal of this research.

5.3.3 Final Copula Selection

In this subsection the final copula selection and the associated motivation is explained. The candidate families with their associated parameters shown in Table 9 are compared based on the goodness-of-fit measures explained in Subsection 5.3.2. The goodness-of-fit results for each location are presented in Tables 28, 29, and 30 in Appendix E.1. Prior to model selection, Spearman's rank correlation coefficient r and its p-value are computed.

France

For France, E_0 and F_p are showing signs that there is no dependency between these two variables. Spearman's r is -0.1003, indicating a weak negative correlation with a p-value of 0.598. This implies a high probability that an uncorrelated dataset could exhibit similar or more extreme dependency, meaning there is no statistically significant dependency between the two variables in France. Table 28 shows the goodness-of-fit results for the different parametric copula families, including the zero parameter independence copula as a baseline. Notably, none of the non-independence families outperforms the independence copula. Clayton and Gumbel match the S_n at 0.527 but have AIC = 2.00, while Gaussian incurs a higher S_n despite marginal AIC gains. Together with the non significant Spearman's r test, it can be assumed the use of an independence copula to model the joint distribution for France.

Portugal

For Portugal the annual heave load F_p and the annual power production E_0 do show a dependency pattern. Spearman's r indicates a weak negative correlation with $r = -0.3437$ and a p-value of 0.0629. The low p-value indicates a statistically significant dependency Table 29 shows that the Gaussian copula has the lowest AIC (-2.071) but the Frank copula yields the best global fit to the empirical copula ($S_n = 0.481$). Both Franks and Gaussian cannot be statistically rejected. The Frank copula is chosen to model the dependence because this study prioritizes the Cramér–von Mises statistic, which directly measures the fit to the empirical copula. In contrast, AIC relies on likelihood offering a more indirect assessment.

Ireland

Ireland shows a positive weak dependence, with Spearman's $r = 0.279$ and a p-value of 0.1226. Because this p-value falls below our threshold of $\alpha = 0.15$, the dependency between these two variables is considered statistically significant in this study. As shown in Table 30, the Frank copula has both the lowest S_n and the lowest AIC, making it the most suitable model for modeling the dependency between variables for Ireland.

6 Results Analysis

After fitting marginal distributions to each of the variables E_0 and F_p and selecting a copula family for France, Portugal, and Ireland, models are simulated from which results are extracted that can be used either for pre-operational site comparison or operational applications. Figure 14 illustrates the structure of this section and shows how each subsection is applied to either the operational or pre-operational phases of the project. First, Subsection 6.1 explains which models are used for the result analysis. Subsection 6.2 describes what results are extracted from the models and how they can be applied in pre-operational site comparison. Finally, Subsection 6.3 focuses on how the models could be used during the operational phase of a wave energy project.

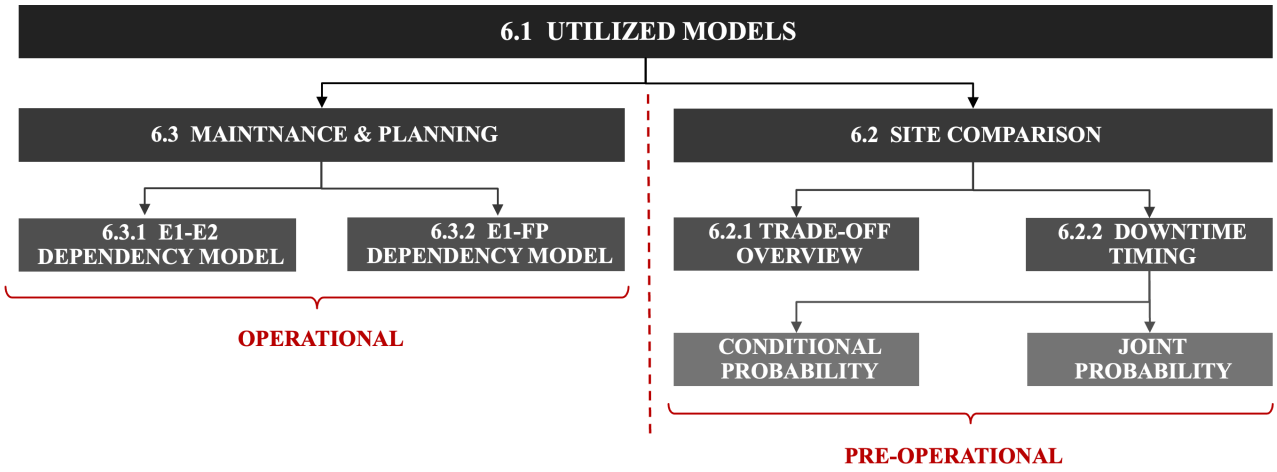

Figure 14: Structure Analysis of Results

6.1 Utilized Models

To analyze the dependence between E_0 and F_p simulated models are established where 10^6 samples are simulated for each location. The samples are simulated in uniform space based on the selected copula (see Subsection 5.3.3). The samples are then mapped back to their original space using the corresponding fitted distributions (see Subsection 5.1). Figure 15 shows the simulated models for each location where each sample within a model represents a pair of annual power production E_0 and peak heave load F_p. The red line indicates the ultimate limit state (ULS) threshold, which is further explained in Subsection 6.1.1.

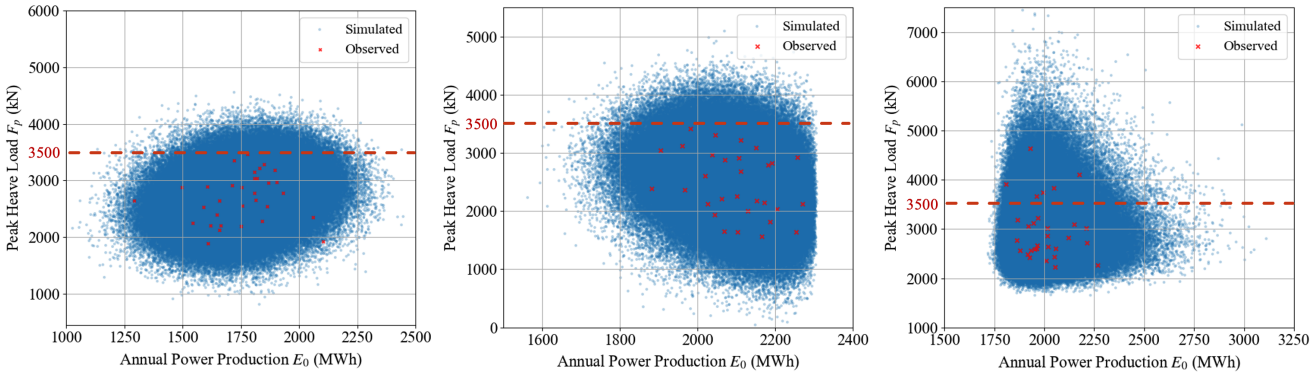

Figure 15: Utilized Models

6.1.1 Ultimate Limit State Threshold

To analyze the probabilities of failure associated to each location in the following Subsections, the focus lies on the maximum resistance of the device and the likelihood of a load exceeding this resistance. Therefore, the peak heave loads that a device experiences at a location are translated to yearly probabilities of failure $P_{yearly,f}$ for the ultimate limit state (ULS). The yearly probability of failure is the likelihood that a peak heave load exceeds a threshold for which the WEC will most likely fail. For this research, the ULS threshold is set to 3500 kN. This value is not based on a specific device's maximum resistance but on most extreme wave events observed. The 3500 kN threshold sits just above the three highest loads observed in Portugal and Ireland corresponding to roughly 12 m waves. Although 3500 kN is not based on the actual resistance of the Corpower inspired wave energy converter, it serves the goal of this research, which is to illustrate how a copula-based framework can be applied.

6.1.2 Yearly Probability of Failure

The target probability of failure $P_{\text{yearly},f}$ is chosen to lie around 1–3 %. The Corpower inspired device has a 20 year design life (DL), so with $P_{\text{yearly},f}$ = 1–3 % the design lifetime probability of failure $P_{f,\text{DL}}$ is 18–45 % (see Equation 26), which could be considered an exemptible risk for such a device. Literature offers no clear guideline on acceptable WEC failure rates because designs vary widely. Therefore, the 1–3 % target zone is an exemplary choice rather than a reflection of an existing offshore renewable design code.

$$P_{f,\text{DL}} = 1 - \left(1 - P_{f,\text{yearly}}\right)^{\text{DL}} \tag{26}$$

6.2 Site Comparison

This Subsection focuses on extracting results from the simulated models shown in Figure 15 and analyzing them such that it enables site-to-site comparison. The goal is to present results that can either replace traditional site comparison methods or provide an additional layer of information. Subsection 6.2.1 presents straightforward averaged results that give a broad overview of the different locations, while Subsection 6.2.2 explores in more depth the use case of the modeled dependency between E_0 and F_p.

6.2.1 Trade-Off Overview

To start the analysis of site comparison, the averaged annual power production $\bar{E}_0$ and yearly probability of failure $P_{\text{yearly},f}$ for the three different locations are compared to each other. This comparison provides a summarizing overview of the conditions at each of the sites, providing the starting point for the analysis. For each of the simulated models in Figure 15, the average annual power production $\bar{E}_0$ and the yearly probability of failure $P_{\text{yearly},f}$ are calculated with equations 27. Here, E_i is the annual power production of sample i, N_{fail} is the number of samples in which the device fails, and N is the total number of simulated yearly samples.

$$\bar{E}_0 = \frac{1}{N}\sum_{i=1}^{N} E_i, \quad P_{\text{yearly},f} = \frac{N_{\text{fail}}}{N} \tag{27}$$

Figure 16 shows the results derived from the simulations and Equation 27 for Portugal, Ireland, and France. The conclusion can immediately be drawn that extreme conditions in France are so severe that the yearly

probability of failure is 14% which is equal to a 95% chance the device will fail during its design life of 20 years. In contrast, both Ireland and Portugal show significantly lower probabilities of failure, with yearly values around 3% and design lifetime probabilities of failure below 45%. Portugal offers the highest average power production and a much lower failure probability than France, making it the most favorable site overall according to this comparison, balancing annual power production and probability of failure.

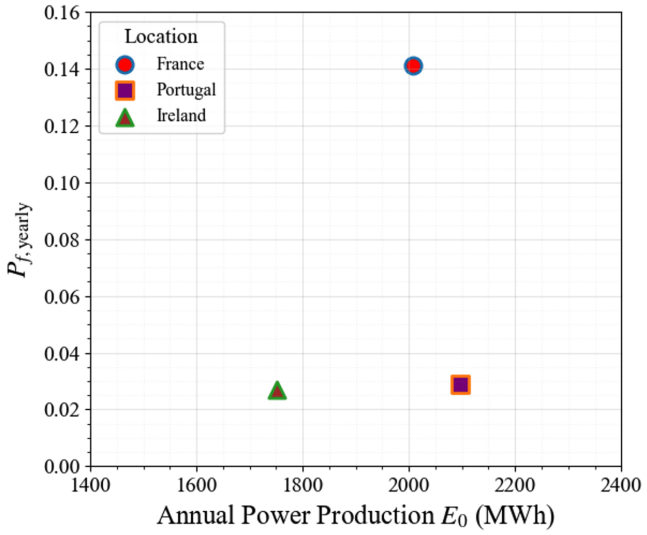

Location	Avg. Power (MWh)	$P_{f,yearly}$	$P_{f,DL}$
France	2007.8	0.141	0.95
Portugal	2097.5	0.029	0.44
Ireland	1752.1	0.027	0.42

Figure 16: Averaged annual power production and yearly probability of failure

These results do not necessarily provide an additional layer of information that traditional site assessment methods cannot reproduce. However, they do provide insight on what it means for the device to be placed at a location, rather than solely focusing on the most extreme return wave. By framing extreme wave risk in terms of probabilistic failure, this approach could offer a more intuitive understanding of site suitability and risk.

In the upcoming subsections, France will be left out of the results analysis because its wave climate is far too extreme. Moreover, these subsections focus on demonstrating the added value of assuming dependence between F_p and E_0. Since France was modeled with an independent copula, its results were uninformative for showing the benefits of the copula approach and therefore did not contribute to the analysis.

6.2.2 Downtime Timing

In Section 2.1 of the literature study, the general site selection criteria used in site comparison studies are analyzed. These studies mostly focus on the wave resource, extreme conditions, and power production. Independence is assumed between these criteria, so each of them is analyzed separately from the others, or their outcomes are combined into a single index (see Subsection **??**). In site comparison studies, none analyze extreme wave conditions and power production together assuming dependence. As a result, it prevents the assessment of how these variables co-occur in a given year and may overlook valuable information. The current framework addresses this gap by using copulas to model the dependence between annual peak heave loads caused by the most severe waves and the corresponding power production for the same year. The results from Subsection 5.3 indicate signs of dependency between these variables, enabling assessment of how this dependence varies across sites. This subsection explores how such differences affect the probability of failure across varying annual power production scenarios, providing an additional layer of information compared to traditional methods that assume independence.

Extreme conditions lead to heavy structural loads on the WEC (F_P in this study), increasing the probability

of failure (Santo et al., 2020) and ultimately leading to higher maintenance costs or downtime (Aderinto and Li, 2018). During operations, downtime resulting from failure can have a significant influence on the overall economic impact. If failure occurs in a low yield year, little revenue is lost. However, if it happens during a high yield year, the most valuable production days or months could be lost, maximizing economic impact. This highlights the importance of failure timing, with more 'convenient' failures occurring in less productive years potentially reducing power production losses. To evaluate this timing aspect, the two probabilistic approaches noted below are considered. Both probabilities are derived empirically from the simulated models shown in Figure 15. Although these probabilities could also be obtained analytically, this approach was not pursued for simplicity. To ensure the empirical results were accurate enough, a comparison was made with analytical results for the conditional probability of failure. The analytical results showed good agreement with those derived empirically from the simulations, suggesting that a sample size of 10^6 is likely sufficient to yield reasonably accurate results.

1. **Conditional Probability of failure:** The conditional yearly failure probability shown in Equation 28 indicates the probability that the peak heave load F_p exceeds the failure threshold f_f, given that the annual power production E_0 falls within a specific energy bin e_b with a width of 25 MWh. This conditional probability is calculated as the ratio of $n_{f,b}$, the number of samples within the energy bin e_b where $F_p \geq f_f$, to n_b, the total number of samples in that bin. In other words, it isolates how risky a particular annual power production scenario is by answering: "If the device produces approximately E_0 MWh in a given year, what is the chance it experiences a failure?"

$$P(F_p \geq f_f \mid E_0 = e_b) = \frac{n_{f,b}}{n_b} \tag{28}$$

2. **Joint Probability of failure:** The joint probability shown in Equation 29 indicates the probability that the annual power production falls within an power production bin and that the device fails. In contrast to the previous conditional probability, it also accounts for how frequently each bin occurs. Bins that occur more often but have a lower conditional failure probability may still have the highest joint probability due to their frequency. This joint probability of failure is calculated by multiplying the conditional probability of failure with the probability that annual power production falls within the bin $P(E_0 = e_b)$, where each bin has a width of 25 MWh. In other words, it answers the question: "What is the overall probability that my device operates in a year with approximately e_b MWh of power production and experiences a failure?"

$$P(F_p \geq f_f \cap E_0 = e_b) = P(F_p \geq f_f \mid E_0 = e_b) \cdot P(E_0 = e_b) \tag{29}$$

It is important to note that both approaches can be valuable, but they differ in how they can be used and the types of questions they could answer. The remainder of this subsection discusses each approach and its application.

Conditional Probability of Failure

Figure 17 shows the relationship between the conditional probability of failure, $P(F_p \geq f_f \mid E_0 = e_b)$, and the annual power production scenario for both Portugal and Ireland, while France is not included. The colored markers represent the probability of the annual power production occurrence, $P(E_0 = e_b)$, indicating how likely it is that the annual power production will fall within a given bin. These plots are based on the simulated samples in Figure 15, where annual power production is divided into 25 MWh bins. The conditional probability of failure for each bin is calculated using Equation 28, and the bin occurrence is estimated as $\frac{n_b}{n}$, with n_b being the total number of samples in a bin and n the total number of simulated samples. Note that the sum of the probability of occurrence $P(E_0 = e_b)$ across all bins for each location equals one. Due to Ireland's more variable annual power production, the distribution spans more bins, each therefore with a lower probability of occurrence.

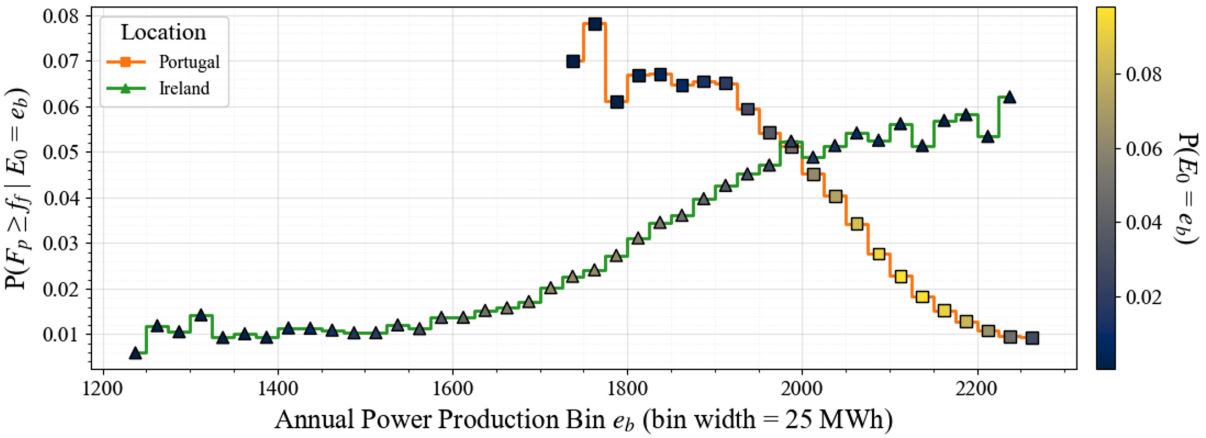

Figure 17: Relationship between conditional probability of failure on the annual energy production

Figure 17 clearly illustrates how the relationship between annual power production and the conditional probability of failure differs between the two locations. For Ireland, the dependence between E_0 and F_p is positive, meaning years with higher power production also tend to have higher loads. As a result, the conditional probability of failure increases with increasing power production. In contrast, Portugal shows a negative dependence, where higher production years are associated with lower peak loads, leading to a lower probability of failure. These observations are consistent with the Spearman's rank correlation coefficient from the observed data ($r = -0.3437$ for Portugal, $r = 0.279$ for Ireland). The fitted copulas capture this behavior by reproducing the observed dependence. For Portugal they assign lower joint probabilities to high E_0 - F_p combinations, while for Ireland they assign higher probabilities to these combinations.

Taking the timing of downtime into account, as discussed earlier in this subsection, this negative correlation is more desirable. It indicates that the probability of failure, and thus the risk of downtime, is minimized during the most productive years, reducing the potential loss of valuable operational time. In contrast, a positive correlation means that probability of failure is higher when operating time is most valuable. This increases the potential economic impact of downtime, as more production could be lost when the system is non-operational. Based on this dependency difference, Ireland becomes less favorable compared to Portugal.

The difference in the relationship between the conditional probability of failure and the annual power production between locations can be directly analyzed to answer the question: "If the device produces approximately E_b MWh, what is the chance it experiences a failure?" This perspective reveals how failure risk shifts with production scenarios, offering insight into the timing of failures. As a result, it adds an additional layer of information beyond traditional methods. However, in this analysis the frequency of bin occurrence is not taken into account. From Figure 17, the frequency of bin occurrence at both the higher and lower energy levels is relatively low. Therefore, it might be that Portugal has a lower probability of failure for higher energy levels, but if these levels are less likely to occur, the argument of positive dependence may not be that interesting due to the low likelihood of ending up in these higher production years. This limitation is addressed in the following approach, where the joint probability of failure is analyzed.

Joint Probability of Failure

Figure 18 shows the relationship between the joint probability of failure $P(F_p \geq f_f \cap E_0 = e_b)$, which combines the bin occurrence $P(E_0 = e_b)$ with the conditional probability of failure $P(F_p \geq f_f | E_0 = e_b)$ (See Equation 29), and the annual power production. The approach answers the question: "What is the probability that my device operates in a year with approximately e_b MWh of power production and experiences failure?". The height of the curves differ because the number of bins varies per location: more bins result in a lower probability of occurrence $P(E_0 = e_b)$ per bin, therefore a lower joint probability of failure. By summing the joint probabilities across all bins at each location, the resulting value corresponds to the yearly probability of failure shown in Figure 16.

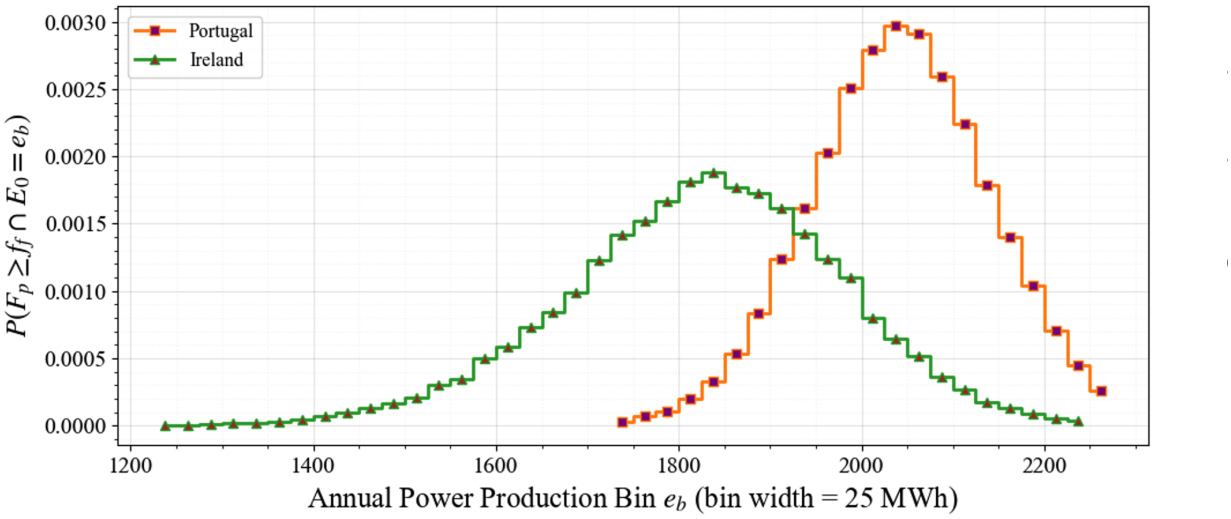

Figure 18: Relationship between the joint probability of failure and the annual power production

The joint probability as shown in Figure 18 provides more information compared to the conditional probability shown in Figure 17, as it also accounts for the frequency of each power production scenario. For example, higher production bins in Ireland may have a high conditional probability of failure, while their probability of occurrence is rather low, resulting in a very low joint probability of failure. This raises the question of how strongly the dependency differences observed in Figure 17 should influence site assessment. While positive dependence may appear unfavorable, the actual chance of simultaneously producing high power and experiencing failure remains very low.

Therefore, only relying on the conditional probability of failure may risk misinterpretation of where the true risk lies if the bin occurrence $P(E_0 = e_b)$ is not considered. Applying the joint probability in site comparison provides a deeper understanding of where failure is most likely to occur. Like the conditional probability, the joint probabilities allow locations to be compared in terms of where failures would have the least economic impact if they occur, but now also considering the frequency of each power production scenario.

The general method for site comparison regarding extreme conditions is discussed in Subsection 2.4.4 of the literature study. This approach typically derives extreme sea scenarios using environmental contours based on the joint distribution of wave height and period. The contour represents sea states associated with a chosen return period, such as 50 years. Sea states along the contour are often used to assess whether the device is likely to withstand the forces induced by these extreme conditions. In other words, general methods mainly focus on the most extreme sea states. For Ireland, the data suggest a positive correlation between E_0 and F_P, meaning there is a general tendency for higher power production years to be associated with higher loads. This suggests that for Ireland, the extreme return wave calculated with the environmental contour method could be associated with the higher power production values shown in Figure 18. However, this plot indicates that the higher contributions to the joint probability of failure are not always located in the tail (highest loads), as their frequency also plays a role.

While the contour approach concentrates on rare, extreme sea states, the joint probability highlights that significant joint probability of failure could arise from less severe extremes loads that occur more frequently. Therefore, Figure 18 not only indicates the power production scenarios where failure is most likely but also shows that these scenarios do not necessarily correspond to the most extreme waves.

6.3 Maintenance and Planning

The previous results provide an additional layer of information for pre-operational site comparison. While pre-operational site comparison is the main scope of this research, two additional dependence models can be applied during operation to estimate the probability of failure for that operational year. The first model, described in Subsection 6.3.1, represents the relationship between the power production in the first and last six months ($E_1 - E_2$). The second model, described in Subsection 6.3.2, represents the relationship between the first six months of power production and the annual peak heave loads (E_1 - F_p). While both models share the same application, each use a different approach.

6.3.1 E_1 - E_2 Dependency Model

This subsection extends the use of conditional failure probability, shown in Figure 17, to the operational phase of a WEC project. As discussed in subsection 6.2.2, the conditional probability of failure $P(F_p \geq f_f | E_0 = e_b)$ provides insights into the probability of failure for each e_b. In this subsection, the focus is on estimating the annual power production range in which an operating WEC is likely to end up at the end of the year, based on the observed power production during the first six months E_1. Once the annual power production range is known in which E_0 is most likely to end up, the conditional probability of failure $P(F_p > f_f \mid E_0 = e_b)$ for that operating year can be evaluated, as it depends on E_0. First, the E_1 - E_2 dependency model used in this estimation is described, and second, the probabilities used for estimating the annual power production range and their application are discussed.

Model

For thirty years of wave data, the observed E_1 and E_2 are determined. The dependency between these two variables is modeled using the same copula modeling approach explained in Section 5. In Ireland, the goodness-of-fit criteria favor a dependent copula, but Spearman's test lacks statistical significance (p-value=0.18), so any assumed dependence should be interpreted with caution. In Portugal, independence cannot be rejected (p-value=0.77). Therefore, Ireland is used here as the reference case for the remainder of this Subsection. For Ireland, the marginal distributions of E_1 and E_2 are each modeled with a normal distribution, parameter estimates (μ, σ) are given in Appendix D.5. Tawn copula is utilized to model the $E_1 - E_2$ dependency. The goodness-of-fit results for the marginal distributions and copula families are provided in Appendix D.4 and E.2.

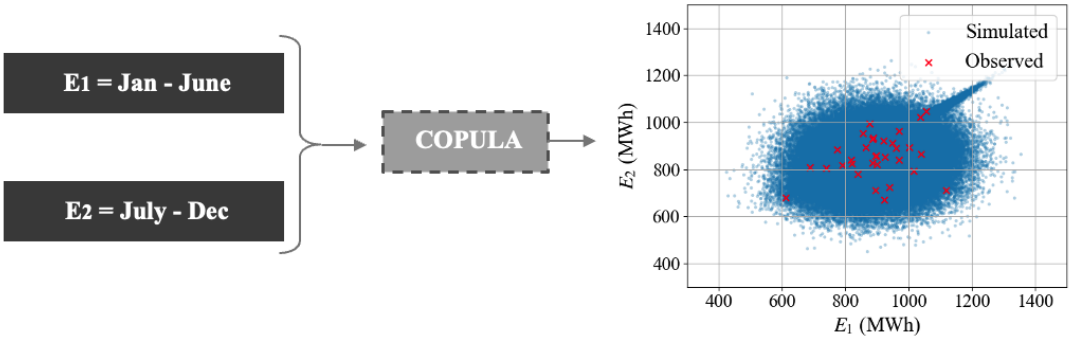

Figure 19: Dependence modeling approach E_1 - E_2

From this model, N^6 pairs of E_1, E_2 are simulated. Figure 19 shows the approach and the final model that is utilized. If during operation e_1 is known, this model can be used to estimate the likelihood of exceeding a total annual power production value for that year (E_0). This step is explained in more detail in the remainder of this subsection.

Conditional Annual power Production Exceedance Probability

If during operation E_1 is known, the model shown in Figure 19 can be used to estimate the likelihood of exceeding a fixed e_0 value for that year. This probability is referred to as the conditional annual power production exceedance probability, expressed in Equation 30.

$$P(E_{1,2} \geq e_0 \mid E_1 = e_1), \qquad E_{1,2} = E_1 + E_2 \tag{30}$$

The conditional annual power production exceedance probability answers the question: "What is the probability that, given e_1 power is produced in the first six months, the total annual power production $E_{1,2}$ will exceed a fixed annual power production e_0?" Figure 20 shows the results of these probabilities, where each line corresponds to a different range of values of e_1.

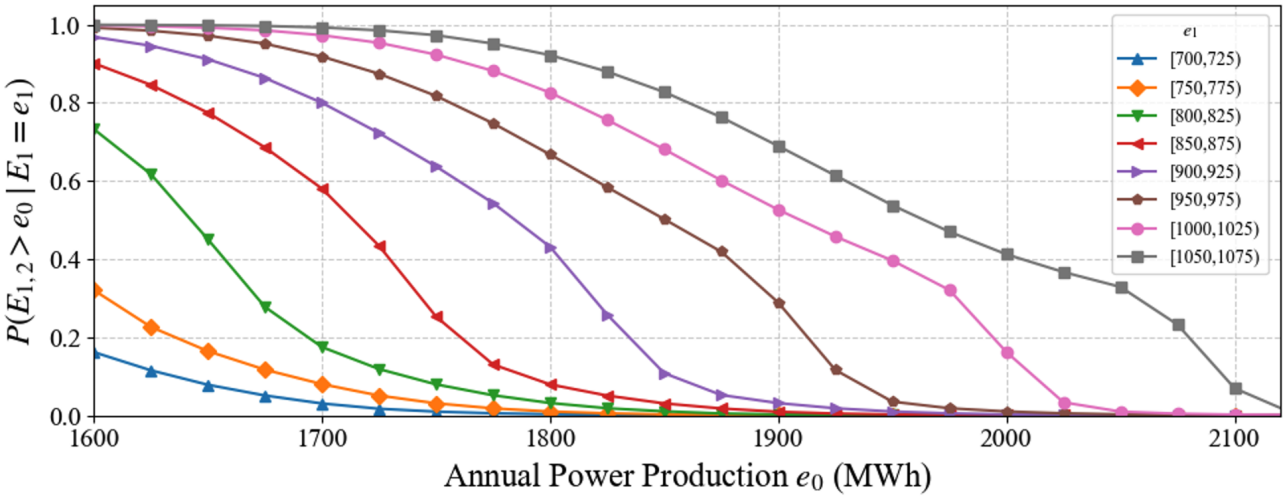

Figure 20: The conditional annual power production exceedance probability for different values of E_1

Knowing the conditional annual power production exceedance probabilities shown in Figure 20 in combination with the conditional failure probabilities shown in Figure 17 could have an useful practical applications in both operational planning and maintenance strategies for a Corpower C4 inspired wave energy converter. An application of the approach is illustrated in the example that follows.

A CorPower C4 inspired device is operating in Ireland. For this location, the conditional probability of failure $P(F_p > f_f \mid E_0 = e_b)$ is known to have a positive dependency with E_0 (see Figure 17). After the first six months of operation, it is measured that $e_1 \approx 1010$ MWh. Figure 20 indicates that for $e_1 \approx 1010$ MWh, the probability of exceeding an annual power production $e_0 \approx 1900$ MWh is around 52% ($P(E_{1,2} \geq 1900 \mid E_1 \approx 1010) \approx 0.52$). Since there is a positive dependence between E_0 and the conditional probability of failure for Ireland, the conditional probability of failure increases as more energy is produced. Figure 17 quantifies this dependence, showing that if $E_0 \geq 1900$MWh, the conditional probability of failure will be at least 4% ($P(F_p \geq f_f \mid E_0 \approx 1900) \approx 0.04$). In other words, during operation it becomes feasible to estimate the probability of failure for that specific operating year. This example demonstrates a case where the probability of failure is on the high side. However, situations could also arise where the estimated conditional probability of failure is on the low side. Understanding the possible range of the conditional probability of failure could enable proactive adjustments in the following areas:

1. **Risk Informed Maintenance Scheduling:** Suppose it is estimated that there is a relatively high risk of exceeding 3500 kN in the second half of the operational year. Operators can plan additional inspections during this period, as the likelihood of encountering a high load event during storms is increased. Conversely, if the risk is low, maintenance activities can be reduced.

2. **Resource Preparation:** Operators can adjust spare parts inventory based on the forecasted risk for the remaining months. This approach avoids overstocking, which wastes capital, and understocking, which can lead to increased downtime when failures occur and parts are unavailable.

The forecast of the conditional probability of failure is limited by uncertainty in predicting the final annual power production E_0. In Ireland, for example, operators might set a guideline to schedule extra inspections when there is roughly a 50% chance of ending up in a high-E_0 range, where failure risk is higher. However, this also means there is still about a 50% chance of ending up in a low-E_0 range, where the extra inspections may not be needed. To avoid this additional step of estimating E_0, the next subsection focuses on directly modeling the relationship between half-year power production E_1 and annual peak heave loads F_p.

6.3.2 E_1 - F_p Dependency Model

To address the limitations of the previous power production dependency model, this subsection focuses on modeling the direct relationship between E_1 and F_p. By leaving E_2 out of the analysis, this approach allows the yearly probability of failure to be calculated solely based on the first six months of power production, yielding a single probability of failure for that year.

Model

For thirty years of wave data, the observed E_1 and F_p are used as input for each of the two locations. The dependency between these two variables is modeled using the same copula modeling approach explained in Section 5. Ireland showed a p-value of 0.086 and a Spearman correlation of 0.308. The corresponding goodness-of-fit tests, including the CvM statistic and AIC, also indicate that some copula models perform reasonably well for Ireland. Portugal showed a p-value of 0.207 and a Spearman correlation of -0.237. The larger p-value and the poor performance in the goodness-of-fit tests suggest that the data do not provide strong evidence for dependence, making any assumption of dependence less reliable. Therefore this Subsection only focuses on Ireland. The goodness-of-fit results for all fitted copula families are presented in Appendix E.3.

A Gaussian copula is chosen to model the dependence between E_1 and F_p for Ireland. Figure 21 shows the approach and the final model, where N^6 pairs of (E_1, F_p) are simulated. The model clearly reveals a positive dependence between power production and peak heave loads, consistent with previous results for Ireland.

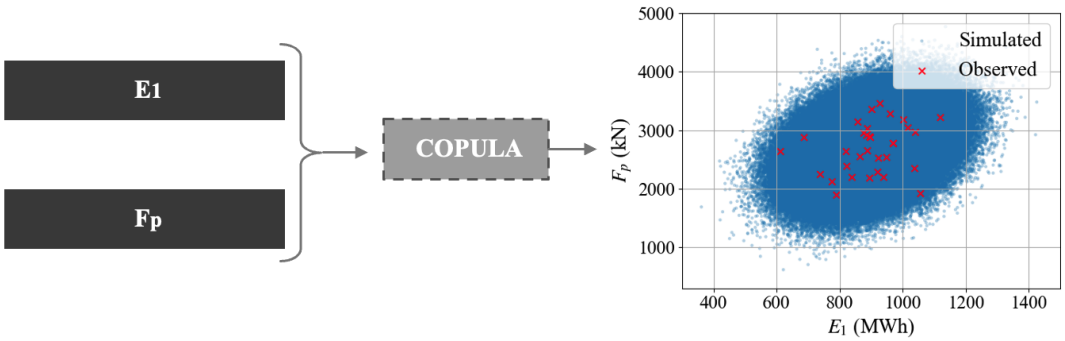

Figure 21: Dependence modeling approach E_1 - F_p

Conditional Probability of Failure

Figure 22 shows the relationship between the conditional probability of failure, $P(F_p \geq f_f \mid E_1 = e_1)$, and the power production of the first six months of an operational year in Ireland. This probability is calculated using Equation 31, where $n_{f,1}$ is the number of samples in an e_1 energy bin (bin width 20 MWh) with $F_p \geq f_f$, and n_1 is the total number of samples in that bin.

$$P(F_p \geq f_f \mid E_1 = e_1) = \frac{n_{f,1}}{n_1} \tag{31}$$

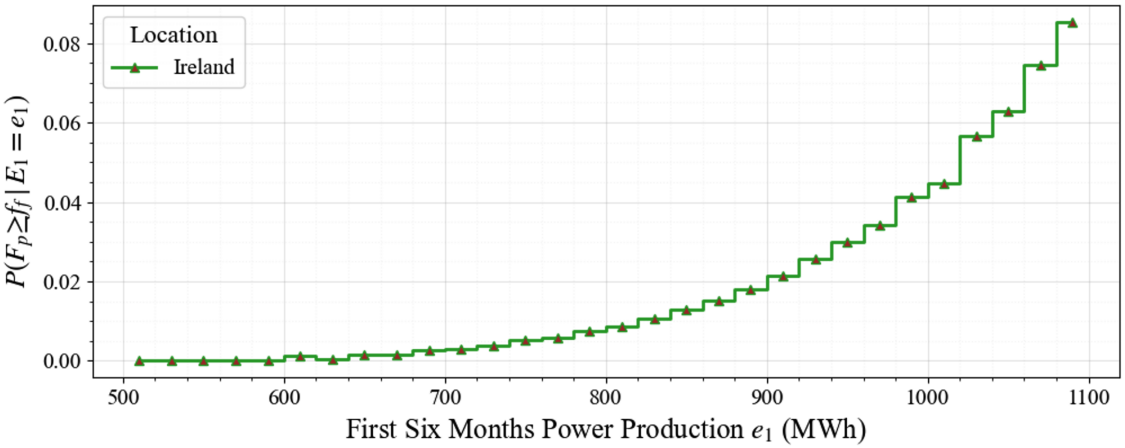

Figure 22: Relationship between E_1 and the conditional failure probability for $f_f = 3500kN$

These results can be applied in the same way as those obtained from the power production dependency model discussed in Subsection 6.3.1. However, Figure 22 allows the yearly probability of failure to be directly determined from the first six months of power production, without the need to estimate E_0. This direct relationship provides a clearer assessment probability of failure, which could offer valuable support for maintenance scheduling and resource preparation during operation.

7 Conclusion

This study focused on developing a novel copula-based framework to evaluate the trade-off between extreme loads and power production while accounting for their dependency, with the aim of laying the groundwork for improving, and potentially replacing, pre-operational site comparison approaches. The proposed framework was also extended with an operational application enabling operators to anticipate periods with a high or low probability of failure. For analysis of the results the probabilities of failure were computed by assuming a maximum heave resistance of $f_f = 3500$ kN, with any exceedance leading to ULS and downtime as a consequence.

For each location, the $F_p - E_0$ dependence was modeled using parametric bivariate copulas. No significant dependence was found for France ($r = -0.100$), while Portugal showed a weak negative ($r = -0.344$) and Ireland a weak positive ($r = 0.279$) dependence. These differences in the sign of the correlation suggested that higher E_0 does not necessarily correspond to higher F_p. A Frank copula was used for Portugal and Ireland to simulate 10^6 (E_0, F_p) pairs per site, forming the basis for different site comparison approaches.

The average annual power production $\overline{E_0}$, the yearly probability of failure $P_{\text{yearly},f}$, and the associated design life ($DL = 20$ years) probability of failure $P_{\text{DL},f}$ were calculated from the simulated pairs to provide an overview of the trade-offs between locations. France exhibited the highest probability of failure($P_{\text{yearly},f} = 14\%$, $P_{\text{DL},f} = 95\%$), making it an undesirable deployment site. Portugal and Ireland showed significantly lower $P_{\text{yearly},f} \approx 3\%$ ($P_{\text{DL},f} \approx 44\%$), with Portugal offering significantly higher $\overline{E_0}$ than Ireland, which made it the most favorable location when balancing $\overline{E_0}$ with $P_{\text{yearly},f}$. France was excluded from the subsequent dependence analysis due to minimal F_p–E_0 correlation and more extreme conditions than Ireland and Portugal.

The analysis of the conditional probability of failure $P(F_p \geq f_f \mid E_0 = e_b)$ showed that, for Ireland, this probability increased during high-production years due to the positive F_p–E_0 dependence, potentially worsening economic impacts when downtime occurs in these high-production periods. In contrast, Portugal showed lower $P(F_p \geq f_f \mid E_0 = e_b)$ in high-production years due to negative F_p–E_0 dependence. This relationship may result in downtime that is potentially less disruptive to the overall profitability of the project. This finding emphasized that Portugal not only offered a more favorable balance between $\overline{E_0}$ and $P_{\text{yearly},f}$, but also benefited from the negative F_p–E_0 dependence.

The previous analysis based on $P(F_p \geq f_f \mid E_0 = e_b)$ did not account for the probability of occurrence of a given annual power production $P(E_0 = e_b)$, as it is conditioned on e_b. To address this, the joint probability of failure $P(F_p \geq f_f \cap E_0 = e_b)$ was analyzed. For both locations the largest contributions to $P(F_p \geq f_f \cap E_0 = e_b)$ come from the most frequently occurring E_0 rather than from the tails of E_0 where $P(E_0 = e_b)$ is the lowest. For Ireland, although high $P(F_p \geq f_f \mid E_0 = e_b)$ is correlated to high E_0, these high E_0 scenarios occur less frequently, limiting their overall contribution to $P(F_p \geq f_f \cap E_0 = e_b)$. In Portugal, the opposite holds. This indicates that, despite differences in dependence patterns shown in $P(F_p \geq f_f \mid E_0 = e_b)$, the primary contributors to $P(F_p \geq f_f \cap E_0 = e_b)$ arise from moderate production years, rather than from tails of E_0, as they are more frequent.

For the E_1–E_2 dependency model, only Ireland showed a weak positive correlation ($r = 0.241$) and Tawn copula was used to model the dependence. The model proved useful for estimating E_0 from early-year production E_1 and linking it to conditional failure probabilities. For example, when $e_1 \approx 1063$ MWh, there is roughly 90% probability that $E_0 \geq 1800$, which corresponds to $P(F_p \geq f_f \mid E_0 \approx 1800) \approx 3\%$. Considering the positive E_0–F_p correlation in Ireland, this implies a 90% likelihood that $P(F_p \geq f_f \mid E_0 = e_b) \geq 3\%$ in that operational year.

For the E_1–F_p dependency model Ireland showed a positive correlation ($r = 0.308$) and was modeled using a Gaussian copula, while Portugal showed no statistically significant correlations and was excluded ($p = 0.207$). The model simulated 10^6 (E_1, F_p) pairs and allowed the estimation of $P(F_p \geq f_f \mid E_1 = e_1)$ directly from E_1 without having to estimate E_0. For Ireland, the results indicate that E_1 is positively correlated with $P(F_p \geq f_f \mid E_1 = e_1)$, offering valuable guidance for proactive maintenance and resource planning directly based on E_1.

8 Discussion

This study proposed a copula-based framework focused on key site comparison criteria that could replace and provide an additional layer of insights compared to conventional pre-operational site comparison assessments. The framework enabled the simulation of samples of key variables (E_0, F_p) for candidate deployment sites taking the dependence between them into account. From these simulated samples three main insights were extracted.

First, the overall trade-off results provided a clear overview of $\overline{E_0}$ versus $P_{\text{yearly},f}$, enabling the reduction of favorable candidate sites. These results could potentially replace conventional methods by summarizing the primary trade-offs between locations. Second, $P(F_p \geq f_f \mid E_0 = e_b)$ introduced an additional layer of insight not captured by conventional approaches. It highlighted how the relationship between E_0 and F_p can influence the desirability of a site by revealing the potential economic impact of downtime. Third, $P(F_p \geq f_f \cap E_0 = e_b)$ clarified how much emphasis should be placed on the $P(F_p \geq f_f \mid E_0 = e_b)$ insights when comparing sites. $P(F_p \geq f_f \mid E_0 = e_b)$ demonstrated that downtime may be more disruptive to project profitability at sites with positive F_p–E_0 dependence compared to those with negative dependence. However, $P(F_p \geq f_f \cap E_0 = e_b)$ shows that failures rarely occur at high E_0 values, implying that the timing effects suggested by $P(F_p \geq f_f \mid E_0 = e_b)$ may be less critical in site comparisons.

These three insights obtained from the copula-based framework served the main purpose of this study by demonstrating that the framework could replace or improve conventional pre-operational site comparison assessments. Besides these three insights, the main conclusion drawn form the probabilistic modeling is that higher E_0 does not necessarily correspond to higher F_p. In other words, favorable power production does not always mean an increased probability of ULS failure. This implies that some sites may experience high operational waves with low extreme waves, whereas others may experience lower operational waves alongside higher extreme waves.

Building on these insights, two additional models were explored to improve operational decision-making: the E_1–E_2 and E_1–F_p dependency models. The E_1 - E_2 dependency model is limited by the uncertainty in predicting E_0, primarily due to the weak correlation observed between E_1 and E_2 for Ireland (p-value = 0.18). Even with a stronger dependence, uncertainty might remain in estimating E_0 based on a observed E_1 value. To overcome this limitation, the dependence model between E_1 and F_p was explored, which demonstrated a statistically significant and positive dependence (p-value = 0.086, r = 0.308) for Ireland, offering a direct way to estimate $P(F_p \geq f_f \mid E_1 = e_1)$ earlier in the operational year enabling operators to adjust maintenance scheduling.

In conventional site comparison assessments, power production is calculated in a similar manner, typically by combining historical sea states with the WEC's power matrix. In contrast, extreme conditions are typically derived from environmental contours based on the joint distribution of wave height and period. This approach is widely used in OFW studies (Li et al., 2017; Li et al., 2019; Li and Zhang, 2020a; Lee et al., 2023; Zhao and Dong, 2023) but also in WEC studies (Edwards and Coe, 2018; Canning et al., 2017; Coe et al., 2018). These contours represent sea states associated with a chosen return period, such as 50 years. Sea states along the contour are used to assess whether the device can withstand the most extreme conditions, focusing mainly on the resource rather than on the probability of failure of a device. Additionally, conventional methods treat power production and extreme return wave scenarios as two independent variables. In cases where these conventional site comparison methods yield similar expected power production and extreme load conditions between sites, they may fail to distinguish which site is more desirable. The copula-based framework showed differences in dependency, offering additional insights that may not always be critical to project profitability but can become decisive when other key factors are similar.

An additional insight from $P(F_p \geq f_f \cap E_0 = e_b)$ is that failures are most likely at mid-range E_0 levels. For Portugal and Ireland, these failures are linked to mid-range F_p values rather than extreme F_p values, reflecting the site-specific E_0–F_p relationships. This suggests that focusing only on extreme loads or waves,

as in conventional methods do, may overlook less extreme scenarios that carry a higher $P(F_p \geq f_f \cap E_0 = e_b)$. While this does not imply a direct shortcoming of the environmental contour method, it highlights the value of comparing both approaches on similar sites in future research. A more detailed comparison could provide insights into how and why their outcomes differ.

This study showed the potential of the copula-based framework. To achieve this within the limited time, simplifications and assumptions were made in the calculation of F_p values used as input for the copula modeling. The load model used a simplified geometry, single-frequency regular waves, linear hydrodynamics, fixed-body assumptions, and neglected pre-tensioning forces. These simplifications introduce potential inaccuracies in the estimation of F_p. While higher-fidelity methods such as time-domain simulations or Computational Fluid Dynamics (CFD) could provide a more realistic representation of loading conditions, their application in this framework is restricted. Generating a sufficiently large dataset to model the dependency between variables would require a large number of simulations, which would require substantial computational time. Instead, future research could focus on more feasible alternatives. For example, hybrid modeling approaches may be adopted, where simplified models are validated against CFD simulations. Another direction could be the use of surrogate models, which can drastically reduce computational costs. Katsidoniotaki et al. (2025) mention the impracticality of extracting statistical load-based information from CFD models and develop a surrogate model as a more efficient alternative, enabling accurate estimation of extreme mooring loads on a WEC with significantly reduced computational cost.

Besides the limitations of the load model, the power production model relied on the power matrix (PM) to estimate power production E_0. The power output for each sea-state bin in the PM was determined by Alday et al. (2023), where several simplifications were made: assuming heave-only motion, neglecting interactions with the wave spring components and the pre-tensioning system, applying suboptimal PTO damping, and assuming deep-water conditions. These assumptions may introduce inaccuracies in the power production estimates. Besides the limitations of the load and power model, the limited sample size of thirty observed (F_p, E_0) pairs introduced several limitations within the framework. These limitations are further discussed in the following paragraphs.

A relatively small sample size of thirty observed annual (H_s, T_p) pairs was used to capture infrequent extreme sea states for calculating F_p. Since the H_s values in these observations needed to fall below the Corpower-inspired cutoff wave height, the PM was reduced from 10.5 meters to 6 meters, ensuring that survival mode was triggered annually for each observation. While this adjustment had a relatively small effect on E_0, it also introduced potential benefits by reducing braking forces through earlier WEC shutdown. However, it raises concerns that the analysis relies on loads that would not typically occur in most operational years. This lack of representativeness may limit how well the results reflect the real operational conditions of the actual device. Additionally, the relatively small sample size resulted in limited statistical significance, which increases the risk of either failing to detect an existing dependency or falsely detecting a dependency between variables. Furthermore, the limited dataset may reduce the accuracy of the fitted parametric marginal distributions. These marginal distributions are critical for mapping simulated samples from the uniform space back to their original scale. If the marginals are inaccurate, they may introduce over- or underestimation of F_p, E_0, E_1, or E_2 in the final simulated samples. The last limitation of the relatively small sample size relates to the framework's ability to account for relevant extreme conditions. By considering only the single most extreme scenario annually, the framework may automatically neglect other events that are nearly as severe as the annual maximum wave. Although these events are slightly less extreme, they may still have the potential to induce failure. Ignoring such scenarios may limits the framework's ability to fully capture the range of extreme loads that should be evaluated.

Although multiple significant extreme events may occur in a given year, the current framework allows only one of them to be paired with E_0. A practical alternative to capture a wider range of extreme loads is to use a single metric that accounts for both the number and magnitude of exceedances. This still enables pairing with E_0 at the annual level. Anderson (1994) introduces such a exceedance based metric.

The other previously mentioned limitations could potentially be addressed by reconsidering the choice of critical component. The braking system protects the PTO and is only loaded in extreme conditions when the device is in survival mode. This limited the framework's flexibility. While extreme loads remain relevant, considering a critical component that is loaded during both operational and extreme conditions with a same type of load could resolve the main limitations. It would remove the need to manipulate the PM, pair loads representative of realistic annual conditions and enable a daily or hourly sample size, improving statistical significance and allowing a wider range of extreme loads to be captured per year. However, if the desire is to keep the braking system as the component of interest, the device used in the framework could be changed to one with a lower cutoff wave height. In this way, the PM may not have to be manipulated, and loads can be paired that are representative of realistic annual conditions. However, the analysis would still rely on relatively infrequent sea states, restricting sample size leading to the earlier mentioned associated limitations.

The final main limitation of this study is the assumption regarding the structural impact of the estimated failure load f_f. It was assumed that reaching $f_f \geq 3500$ kN would cause ULS failure and lead to significant downtime. This was necessary, as a detailed analysis of structural consequences was beyond the scope of this study. Future research could focus more on the consequences of different values of f_f on a system. This would allow failures to be classified into multiple types, beyond just ULS. For example, the SLS (Serviceability Limit State) associated with f_f could be analyzed, where the device would require maintenance but not necessarily experience downtime. ULS (Ultimate Limit State), in contrast, concerns more severe failures. If multiple failure modes linked to specific f_f thresholds are known, it becomes feasible to extract corresponding probabilities of failure for each mode from the same simulated models. This would refine the analysis by providing insights into the probability of failure for multiple distinct failure modes beyond just ULS, each with different consequences for the economic viability of a project.

A limitation of the operational E_1–E_2 and E_1–F_p dependency models is that they estimate a low ULS failure probability across a broad time window. This could restricts their effectiveness in guiding timely maintenance decisions. If failure probabilities were available at a higher temporal resolution, maintenance scheduling could be more effectively targeted. Additionally, focusing on more frequent loads would offer more reliable indicators, reducing the risk of unnecessary maintenance. For example, if weekly pairs were modeled and one week of power production indicated a 70% probability of SLS failure in the following week, scheduling maintenance would be more justified than in a scenario where there is only a 7% likelihood of ULS failure occurring at some point over the next six months.

A Power Model Results

A.1 Annual Power Production Values

Year	E_0 (MWh)	CF (%)	**Year**	E_0 (MWh)	CF (%)	**Year**	E_0 (MWh)	CF (%)
1992	2266.6	64.5	**2002**	2149.3	61.3	**2012**	2057.4	58.6
1993	2018.8	57.6	**2003**	1963.2	56.0	**2013**	2055.6	58.7
1994	1992.4	56.9	**2004**	1950.9	55.5	**2014**	1930.0	55.1
1995	1862.7	53.2	**2005**	1877.5	53.6	**2015**	2215.0	63.2
1996	1944.5	55.3	**2006**	1931.9	55.1	**2016**	2047.8	58.3
1997	1928.2	55.0	**2007**	1807.6	51.6	**2017**	1960.7	56.0
1998	1967.8	56.2	**2008**	2174.3	61.9	**2018**	2120.3	60.5
1999	2052.7	58.6	**2009**	1965.6	56.1	**2019**	2016.3	57.5
2000	2010.0	57.2	**2010**	1866.5	53.3	**2020**	2017.1	57.4
2001	1917.9	54.7	**2011**	2209.9	63.1	**2021**	1919.4	54.8

Table 10: Annual power production and CF for France

Year	E_0 (MWh)	CF (%)	**Year**	E_0 (MWh)	CF (%)	**Year**	E_0 (MWh)	CF (%)
1992	2171.3	61.8	**2002**	2256.8	64.4	**2012**	2068.7	58.9
1993	2186.2	62.4	**2003**	1960.5	55.9	**2013**	2269.7	64.8
1994	2101.4	60.0	**2004**	2103.6	59.9	**2014**	2046.5	58.4
1995	2166.2	61.8	**2005**	1966.9	56.1	**2015**	2253.4	64.3
1996	2038.0	58.0	**2006**	2044.2	58.3	**2016**	2151.6	61.2
1997	2071.2	59.1	**2007**	1881.6	53.7	**2017**	1903.9	54.3
1998	1981.1	56.5	**2008**	2110.8	60.1	**2018**	2191.5	62.5
1999	2106.7	60.1	**2009**	2062.2	58.9	**2019**	2151.5	61.4
2000	2129.8	60.6	**2010**	2111.7	60.3	**2020**	2205.5	62.8
2001	2020.3	57.7	**2011**	2181.2	62.2	**2021**	2026.0	57.8

Table 11: Annual power production and CF for Portugal

Year	E_0 (MWh)	CF (%)	**Year**	E_0 (MWh)	CF (%)	**Year**	E_0 (MWh)	CF (%)
1990	1903.5	54.3	**2000**	1757.2	50.0	**2010**	1291.6	36.9
1991	1779.3	50.8	**2001**	1607.7	45.9	**2011**	2060.1	58.8
1992	2103.0	59.9	**2002**	1830.6	52.2	**2012**	1657.2	47.2
1993	1721.3	49.1	**2003**	1662.9	47.5	**2013**	1711.7	48.9
1994	1807.9	51.6	**2004**	1750.5	49.8	**2014**	1850.7	52.8
1995	1591.0	45.4	**2005**	1495.8	42.7	**2015**	1896.7	54.1
1996	1543.6	43.9	**2006**	1657.7	47.3	**2016**	1820.1	51.8
1997	1619.4	46.4	**2007**	1605.8	45.8	**2017**	1841.3	52.5
1998	1809.7	51.6	**2008**	1869.9	53.2	**2018**	1932.1	55.1
1999	1862.3	53.1	**2009**	1808.8	51.6	**2019**	1754.7	50.1

Table 12: Annual power production and CF for Ireland

B Load Model Results

B.1 Extreme Sea States

Year	$H_s(m)$	$T_p(s)$	**Year**	$H_s(m)$	$T_p(s)$	**Year**	$H_s(m)$	$T_p(s)$
1992	8.33	17.86	**2002**	11.06	19.61	**2012**	9.86	16.39
1993	10.02	17.86	**2003**	9.15	20.83	**2013**	9.66	12.66
1994	13.75	17.86	**2004**	10.48	14.29	**2014**	16.77	18.87
1995	11.39	13.89	**2005**	10.57	13.70	**2015**	10.19	16.95
1996	11.40	18.18	**2006**	9.66	16.67	**2016**	13.42	21.28
1997	10.01	13.70	**2007**	14.32	18.18	**2017**	13.23	18.87
1998	12.18	16.67	**2008**	14.75	19.23	**2018**	10.37	17.86
1999	10.50	12.82	**2009**	10.10	16.39	**2019**	10.17	20.00
2000	9.67	13.89	**2010**	11.72	17.86	**2020**	11.51	16.13
2001	9.15	17.86	**2011**	10.53	21.74	**2021**	11.33	17.54

Table 13: Annual maximum significant wave height and concomitant peak period France

Year	$H_s(m)$	$T_p(s)$	**Year**	$H_s(m)$	$T_p(s)$	**Year**	$H_s(m)$	$T_p(s)$
1992	8.26	15.87	**2002**	10.47	19.61	**2012**	6.26	16.39
1993	7.81	12.82	**2003**	11.40	18.18	**2013**	8.08	16.39
1994	8.92	14.93	**2004**	7.26	12.35	**2014**	11.43	22.73
1995	7.42	11.24	**2005**	8.43	20.00	**2015**	6.78	13.70
1996	10.67	19.23	**2006**	8.02	13.70	**2016**	7.76	20.00
1997	10.23	20.00	**2007**	8.58	19.23	**2017**	10.93	19.23
1998	12.10	20.41	**2008**	11.77	18.18	**2018**	10.73	16.39
1999	10.35	20.00	**2009**	8.68	15.15	**2019**	10.97	20.41
2000	7.38	17.86	**2010**	9.77	18.52	**2020**	8.16	14.49
2001	9.41	18.87	**2011**	10.59	16.39	**2021**	7.54	20.00

Table 14: Annual maximum significant wave height and concomitant peak period Portugal

Year	H_s(m)	T_p(s)	**Year**	H_s(m)	T_p(s)	**Year**	H_s(m)	T_p(s)
1990	11.02	17.45	**2000**	9.81	15.86	**2010**	10.15	15.86
1991	12.45	19.19	**2001**	8.86	17.45	**2011**	9.02	15.86
1992	8.15	13.19	**2002**	11.93	17.45	**2012**	8.15	15.86
1993	12.45	17.45	**2003**	7.93	19.19	**2013**	10.82	17.45
1994	10.93	19.19	**2004**	8.43	15.86	**2014**	11.81	19.19
1995	9.36	17.45	**2005**	10.35	19.19	**2015**	11.45	19.19
1996	9.06	14.27	**2006**	10.16	15.86	**2016**	10.90	19.19
1997	8.46	17.45	**2007**	10.73	17.45	**2017**	8.80	15.86
1998	11.66	17.45	**2008**	10.98	17.45	**2018**	10.32	17.45
1999	9.76	15.86	**2009**	10.32	17.45	**2019**	10.62	17.45

Table 15: Annual maximum significant wave height and concomitant peak period Ireland

B.2 Peak Heave loads

Year	$H_s(m)$	$T_p(s)$	$F_p(kN)$	**Year**	$H_s(m)$	$T_p(s)$	$F_p(kN)$	**Year**	$H_s(m)$	$T_p(s)$	$F_p(kN)$
1992	8.33	17.86	2265	**2002**	11.06	19.61	3093	**2012**	9.86	16.39	2599
1993	10.02	16.39	2641	**2003**	9.15	20.83	2599	**2013**	9.66	12.66	2226
1994	13.75	17.86	3738	**2004**	10.48	14.29	2595	**2014**	16.77	18.87	4639
1995	11.39	13.89	2778	**2005**	10.57	13.70	2558	**2015**	10.19	16.95	2720
1996	11.4	18.18	3118	**2006**	9.66	16.67	2563	**2016**	13.42	21.28	3831
1997	10.01	13.70	2422	**2007**	14.32	18.18	3916	**2017**	13.23	18.87	3660
1998	12.18	16.67	3231	**2008**	14.75	19.23	4103	**2018**	10.37	17.86	2820
1999	10.5	12.82	2440	**2009**	10.10	16.39	2662	**2019**	10.17	20.00	2859
2000	9.67	13.89	2358	**2010**	11.72	17.86	3187	**2020**	11.51	16.13	3014
2001	9.15	17.86	2488	**2011**	10.53	21.74	3021	**2021**	11.33	17.54	3062

Table 16: Annual peak heave load France

Year	H_s(m)	T_p(s)	F_p(kN)	**Year**	H_s(m)	T_p(s)	F_p(kN)	**Year**	H_s(m)	T_p(s)	F_p(kN)
1992	8.26	15.87	2148	**2002**	10.47	19.61	2927	**2012**	6.26	16.39	1650
1993	7.81	12.82	1816	**2003**	11.40	18.18	3118	**2013**	8.08	16.39	2129
1994	8.92	14.93	2257	**2004**	7.26	12.35	1644	**2014**	11.43	22.73	3311
1995	7.42	11.24	1563	**2005**	8.43	20.00	2369	**2015**	6.78	13.70	1641
1996	10.67	19.23	2968	**2006**	8.02	13.70	1941	**2016**	7.76	20.00	2182
1997	10.23	20.00	2876	**2007**	8.58	19.23	2387	**2017**	10.93	19.23	3041
1998	12.10	20.41	3420	**2008**	11.77	18.18	3218	**2018**	10.73	16.39	2829
1999	10.35	20.00	2910	**2009**	8.68	15.15	2211	**2019**	10.92	20.41	3087
2000	7.38	17.86	2006	**2010**	9.77	18.52	2688	**2020**	8.16	14.49	2035
2001	9.41	18.87	2602	**2011**	10.59	16.39	2791	**2021**	7.54	20.00	2120

Table 17: Annual peak heave load Portugal

Year	H_s(m)	T_p(s)	F_p(kN)	**Year**	H_s(m)	T_p(s)	F_p(kN)	**Year**	H_s(m)	T_p(s)	F_p(kN)
1990	11.02	17.45	2971	**2000**	9.81	15.86	2551	**2010**	10.15	15.86	2639
1991	12.45	19.19	3461	**2001**	8.86	17.45	1894	**2011**	9.02	15.86	2346
1992	8.15	13.19	1921	**2002**	11.93	17.45	3217	**2012**	8.15	15.86	2121
1993	12.45	17.45	3358	**2003**	7.93	19.19	2203	**2013**	10.82	17.45	2918
1994	10.93	19.19	3093	**2004**	8.43	15.86	2191	**2014**	11.81	19.19	3282
1995	9.36	17.45	2526	**2005**	10.34	19.19	2875	**2015**	11.45	19.19	3184
1996	9.06	14.27	2253	**2006**	10.16	15.86	2642	**2016**	10.90	19.19	3033
1997	8.46	15.86	2200	**2007**	10.73	17.45	2894	**2017**	8.80	15.86	2288
1998	11.66	17.45	3145	**2008**	10.98	17.45	2962	**2018**	10.32	17.45	2783
1999	9.76	15.86	2537	**2009**	10.32	17.45	2783	**2019**	10.62	17.45	2876

Table 18: Annual peak heave load Ireland

C Fitted Marginal Distributions Per Location

- **Ireland:** The annual peak heave load histogram shown on the left in Figure 23, peaks near 2600–2800 kN and seems to show a light negative skew towards 3400 kN. Gamma and Log-Normal address the light negative skew, the Normal provides a symmetric baseline, and GEV and GumbelMin model the more extreme lower load behavior. The annual powerproduction histogram shown on the right in Figure 23, centers around 1700–1800 MWh and exhibits a light negative skew. To model the moderate asymmetry, Normal, Gamma, and Log-Normal fits are applied, while GumbelMin captures the slightly heavier left tail.

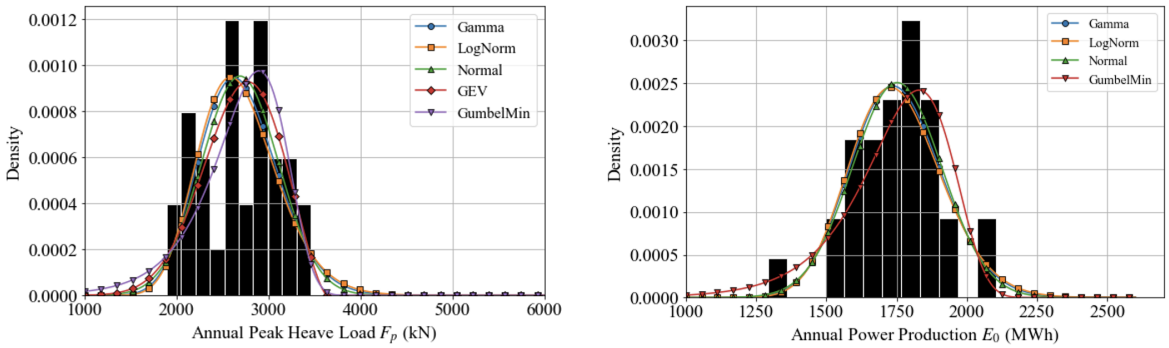

Figure 23: Histograms and fitted parametric distributions for Ireland

- **Portugal:** The annual peak heave load histogram shown on the left in Figure 24, peaks near 1600–2250 kN and seems to show a light positive skew towards 3400 kN. Gamma and Log-Normal address the light positive skew, the Normal provides a symmetric baseline, and Gumbel Max models the extreme high-load behavior. The annual power production shown on the right in Figure 24, centers around 2000–2200 MWh with a mild left skew, suggesting Normal, Gamma and Log-Normal fits for the bulk and moderate asymmetry, while Gumbel Min and GEV capture the slightly heavier left tail.

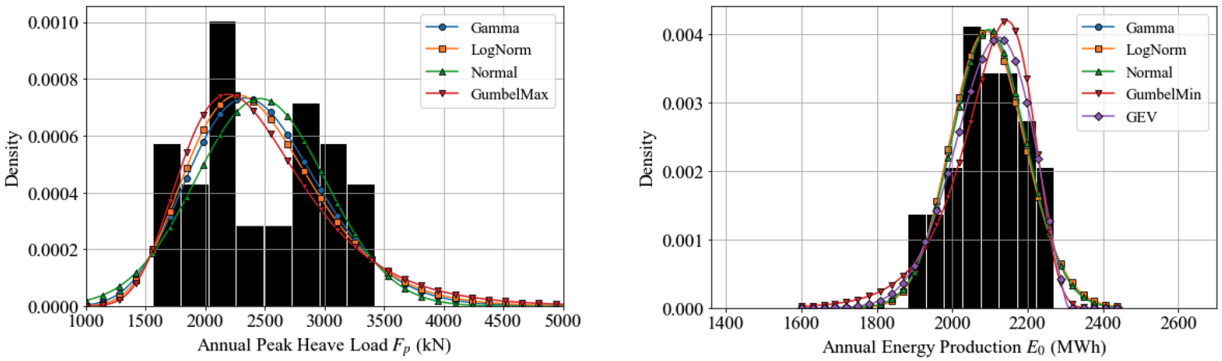

Figure 24: Histograms and fitted parametric distributions for Portugal

- **France:** The annual peak heave load histogram shown on the left in Figure 25 peaks near 2000 kN-3000 kN, with a clear right hand tail stretching out past 4500 kN. Gamma and Log-Normal both possess that same moderate positive skew and so hug the body of the distribution. The Normal provides a simple symmetric baseline for comparison, while Gumbel Max presents a more asymmetric behavior in the extreme upper-tail capturing the behavior of the variable better than the other three distributions. The annual power production histogram shown on the right in Figure 25, peaks near between 1800 MWh-2100 MWh with a milder right skew. Again, Gamma and Log-Normal reproduce that slight asymmetry, the Normal gives a midpoint reference, and Gumbel Max is applied to model slightly more asymmetric behavior compared to the other distributions.

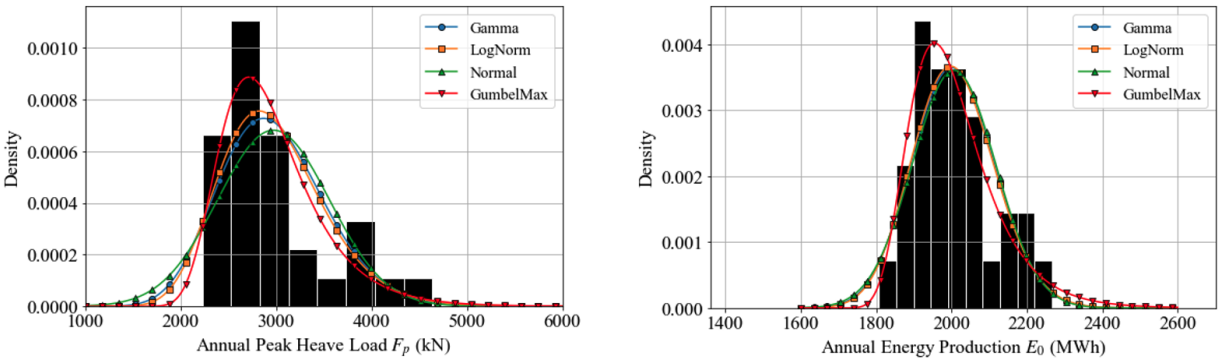

Figure 25: Histograms and fitted parametric distributions for France

D Marginal Distribution GoF Results

D.1 QQ plots

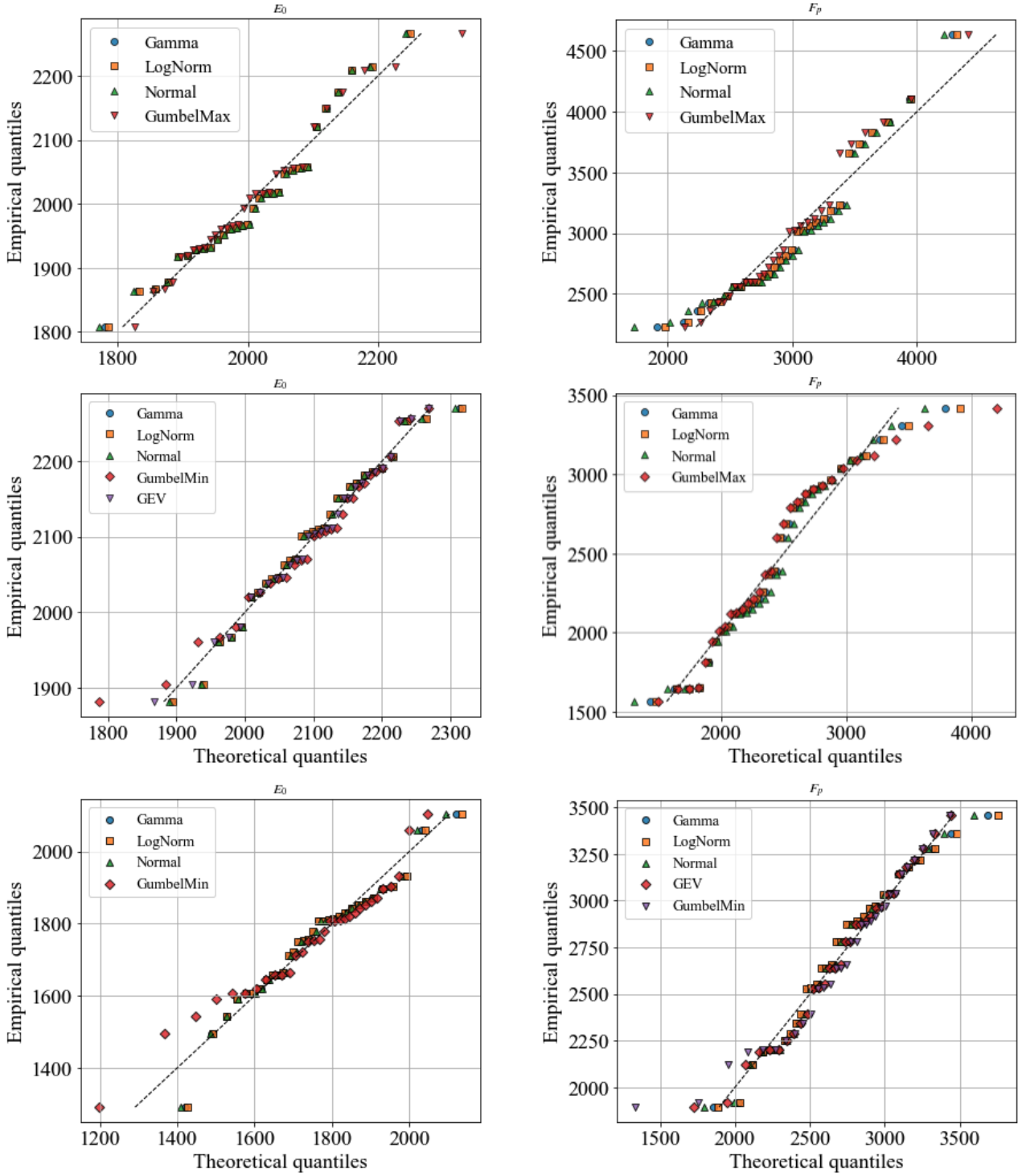

Figure 26: QQ plots for the variables E_o (left column) and F_p (right column), for France (top row), Portugal (mid row), and Ireland (bottom row)

D.2 Log-scale exceedance plots

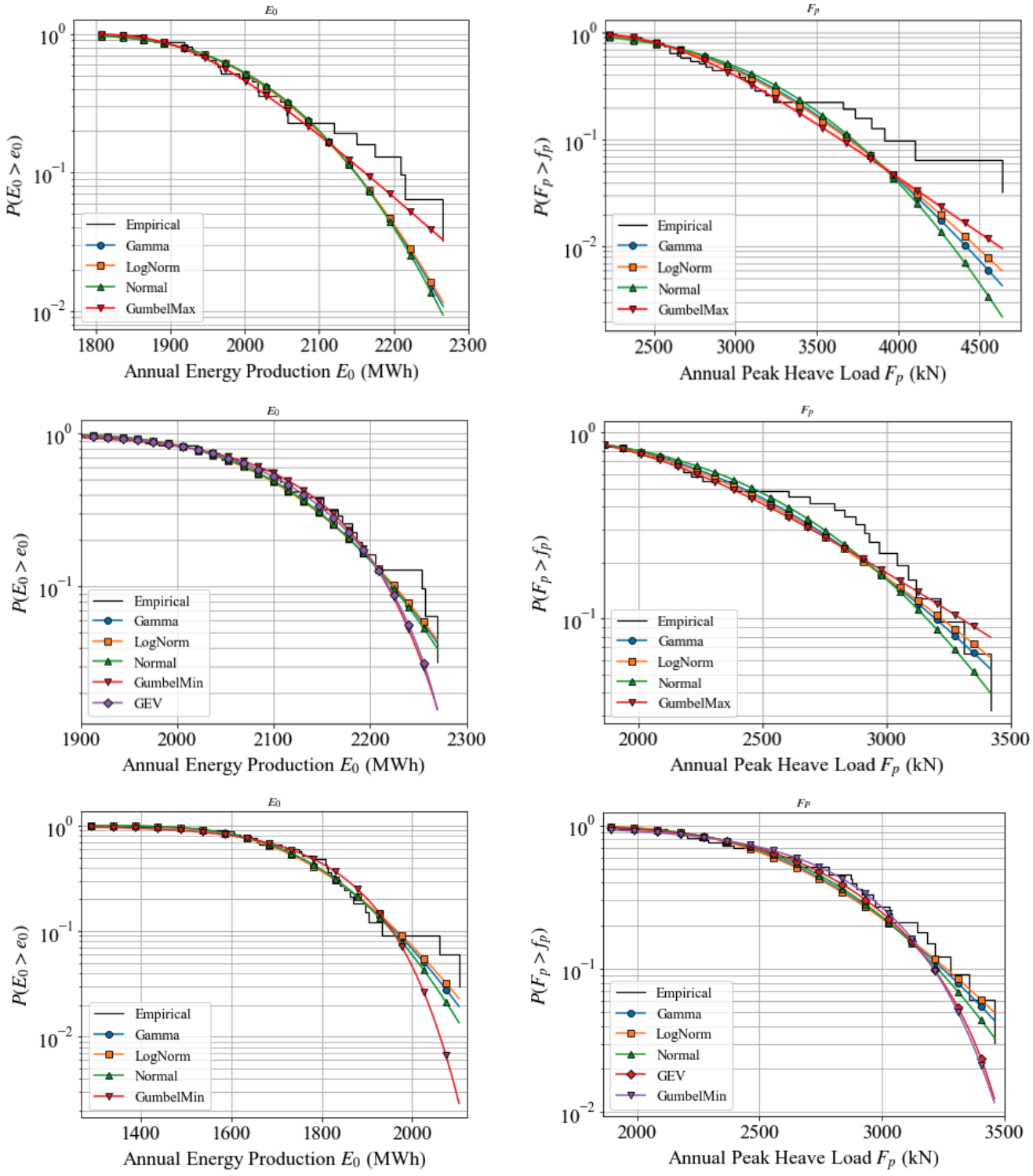

Figure 27: log-scale exceedance plots for the variables E_0 (left column) and F_p (right column), for France (top row), Portugal (mid row), and Ireland (bottom row)

D.3 GoF KS Results for Variables E_0 and F_p

Distribution	Variable	D_n	p-value
Gamma	E_0	0.133	0.62
Log Norm	E_0	0.130	0.64
normal	E_0	0.137	0.58
Gumbel Max	E_0	0.090	0.95

Table 19: E_0 Goodness-of-fit results France

Distribution	Variable	D_n	p-value
Gamma	F_p	0.130	0.64
Log Norm	F_p	0.127	0.68
normal	F_p	0.145	0.51
Gumbel Max	F_p	0.112	0.81

Table 20: F_p Goodness-of-fit results France

Distribution	Variable	D_n	p-value
Gamma	E_0	0.089	0.95
Log Norm	E_0	0.092	0.94
normal	E_0	0.083	0.97
Gumbel Min	E_0	0.105	0.86
GEV	E_0	0.075	0.99

Table 21: E_0 Goodness-of-fit results Portugal

Distribution	Variable	D_n	p-value
Gamma	F_p	0.139	0.56
Log Norm	F_p	0.144	0.51
normal	F_p	0.126	0.68
Gumbel Max	F_p	0.144	0.52

Table 22: F_p Goodness-of-fit results Portugal

Distribution	Variable	D_n	p-value
Gamma	E_0	0.114	0.76
Log Norm	E_0	0.117	0.73
normal	E_0	0.106	0.83
Gumbel Min	E_0	0.115	0.75

Table 23: E_0 Goodness-of-fit results Ireland

Distribution	Variable	D_n	p-value
Gamma	F_p	0.119	0.71
Log Norm	F_p	0.125	0.65
normal	F_p	0.107	0.82
GEV	F_p	0.082	0.97
Gumbel Min	F_p	0.089	0.94

Table 24: F_p Goodness of fit results Ireland

D.4 GoF KS Results for Variables E_1 and E_2

Distribution	Variable	D_n	p-value
Gamma	E_1	0.127	0.640
Log Norm	E_1	0.135	0.560
normal	E_1	0.109	0.801
Gumbel Max	E_1	0.158	0.362

Table 25: E_1 Goodness-of-fit results Ireland

Distribution	Variable	D_n	p-value
Gamma	E_2	0.092	0.928
Log Norm	E_2	0.098	0.893
normal	E_2	0.081	0.974
Gumbel Max	E_2	0.141	0.505

Table 26: E_2 Goodness-of-fit results Ireland

D.5 Parameter Estimates Marginal Distributions for Variables E_1 and E_2

Location	Variable	Distribution	p-value	Parameter	Notation	Value
Ireland	E_1	Normal (σ_N, μ_N)	0.80	Mean	μ_N	898.5
				Standard deviation	σ_N	105.6
Ireland	E_2	Normal (σ_N, μ_N)	0.97	Mean	μ_N	853.5
				Standard deviation	σ_N	92.3

Table 27: Fitted parametric distributions E_1 and E_2

E Copula Families GoF Results

E.1 CvM and AIC for E_0 - F_p Copula

Copula Family	**Parameters**	S_n	AIC
Gaussian	$C_{\text{ga}}(u, v; -0.21)$	1.434	1.115
Student-t	$C_{st}(u, v; -0.11, 4.00)$	0.842	2.913
Clayton	$C_{\text{cl}}(u, v; 1.8 \cdot 10^{-6})$	0.527	2.000
Frank	$C_{\text{fr}}(u, v; -0.67)$	0.959	1.686
Gumbel	$C_{\text{gu}}(u, v; 1.00)$	0.527	2.000
Independence	-	0.527	0.0

Table 28: Goodness-of-fit E_0 - F_p Copula Results - France

Copula Family	**Parameters**	S_n	AIC
Gaussian	$C_{\text{ga}}(u, v; -0.42)$	0.695	-2.071
Student-t	$C_{st}(u, v; -0.41, 50.0)$	0.668	0.090
Clayton	$C_{\text{cl}}(u, v; 1.8 \cdot 10^{-6})$	0.556	2.000
Frank	$C_{\text{fr}}(u, v; -2.20)$	0.481	-1.484
Gumbel	$C_{\text{gu}}(u, v; 1.00)$	0.556	2.000
Independence	-	0.556	0.0

Table 29: Goodness-of-fit E_0 - F_p Copula Results - Portugal

Copula Family	**Parameters**	S_n	AIC
Gaussian	$C_{\text{ga}}(u, v; 0.24)$	0.862	0.745
Student-t	$C_{st}(u, v; 0.28, 8.70)$	0.723	2.481
Clayton	$C_{\text{cl}}(u, v; 0.42)$	0.723	0.085
Frank	$C_{\text{fr}}(u, v; 1.80)$	0.603	-0.467
Gumbel	$C_{\text{gu}}(u, v; 1.20)$	0.998	1.088
Independence	-	2.311	0.0

Table 30: Goodness-of-fit E_0 - F_p Copula Results - Ireland

E.2 CvM and AIC for E_1 - E_2 Copula

Copula Family	**Parameters**	S_n	AIC
Gaussian	$C_{\text{ga}}(u, v; 0.33)$	0.478	-0.510
Student-t	$C_{st}(u, v; 0.28, 2.2)$	0.497	-0.581
Clayton	$C_{\text{cl}}(u, v; 0.46)$	0.509	-0.421
Frank	$C_{\text{fr}}(u, v; 1.7)$	0.578	-0.047
Gumbel	$C_{\text{gu}}(u, v; 1.3)$	0.501	-1.580
Tawn	$C_{\text{gu}}(u, v, w; 0.3, 0.6, 7)$	0.411	-3.499
Independence	-	2.906	0.0

Table 31: Goodness-of-fit E_1 - E_2 Copula Results - Ireland

E.3 CvM and AIC for E_1 - F_p Copula

Copula Family	**Parameters**	S_n	AIC
Gaussian	$C_{\text{ga}}(u, v; 0.35)$	0.258	-0.959
Student-t	$C_{st}(u, v; 0.35, 8.9)$	0.258	0.807
Clayton	$C_{\text{cl}}(u, v; 0.49)$	0.409	-0.575
Frank	$C_{\text{fr}}(u, v; 2.1)$	0.281	-1.193
Gumbel	$C_{\text{gu}}(u, v; 1.3)$	0.360	-0.733
Independence	-	2.123	0.0

Table 32: Goodness-of-fit E_1 - F_p Copula Results - Ireland

Copula Family	**Parameters**	S_n	AIC
Gaussian	$C_{\text{ga}}(u, v; -0.24)$	0.883	0.792
Student-t	$C_{st}(u, v; -0.25, 50)$	0.893	2.812
Clayton	$C_{\text{cl}}(u, v; 1.8 \cdot 10^{-6})$	0.544	2.00
Frank	$C_{\text{fr}}(u, v; -1.5)$	0.890	0.385
Gumbel	$C_{\text{gu}}(u, v; 1)$	0.544	2.00
Independence	-	2.123	0.0

Table 33: Goodness-of-fit E_1 - F_p Copula Results - Portugal

E.4 Quadrant Semi-Correlations Portugal

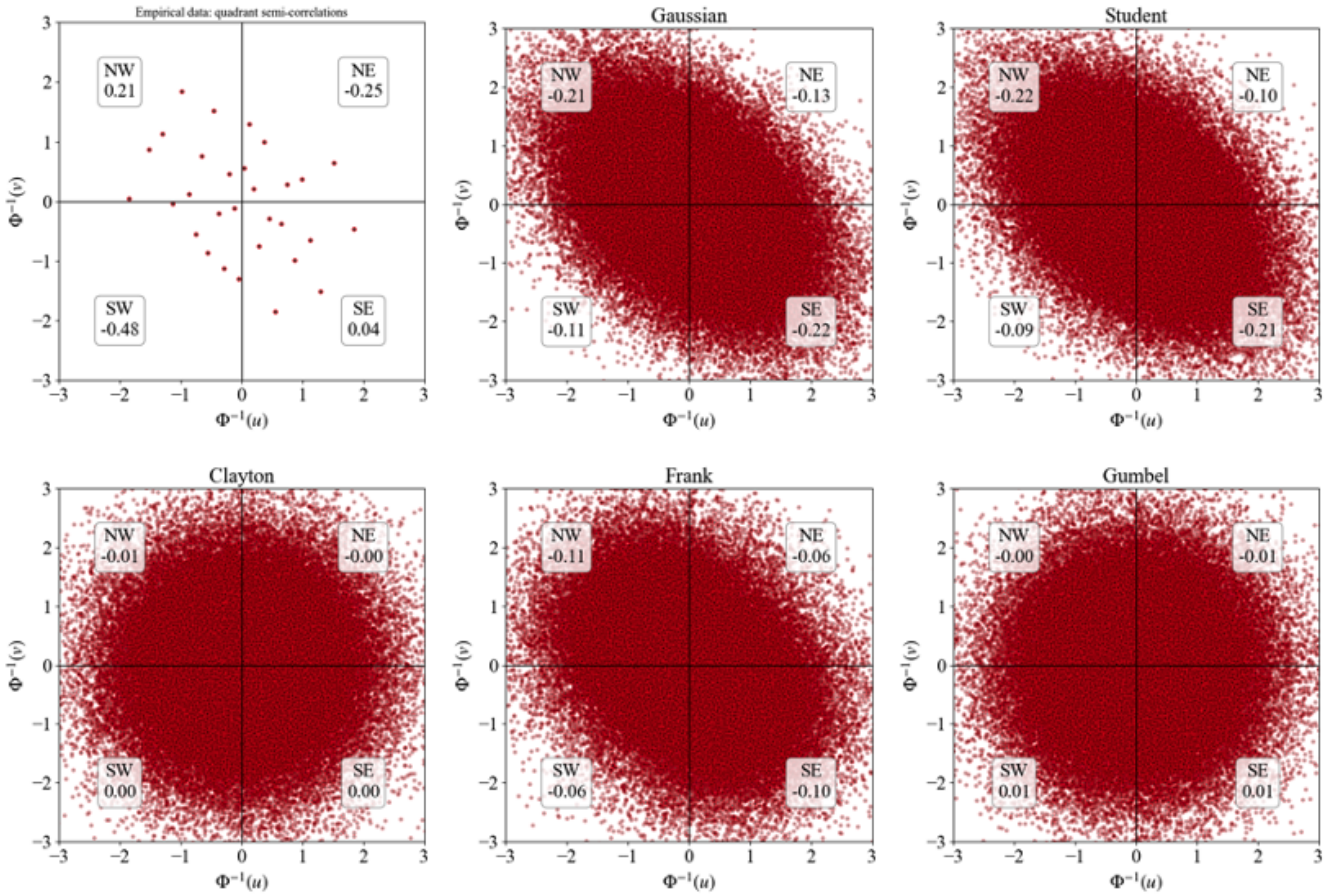

Figure 28: Semi-correlations Portugal

F Marginal Distributions Candidates - PDF Equations

- **Gamma:**

$$f(x;\alpha,\mu,\beta) = \frac{1}{\beta^{\alpha}\,\Gamma(\alpha)}(x-\mu)^{\alpha-1}\exp\left(-\frac{x-\mu}{\beta}\right)$$

  - α represents the shape parameter
  - μ represents the the location parameter
  - β represents the scale parameter

- **Lognorm:**

$$f(x;\sigma,\mu,\beta) = \frac{1}{(x-\mu)\,\sigma\sqrt{2\pi}}\exp\left(-\frac{\left(\log\left(\frac{x-\mu}{\beta}\right)\right)^2}{2\sigma^2}\right)$$

  - σ represents the shape parameter
  - μ represents the the location parameter
  - β represents the scale parameter

- **Normal:**

$$f(x;\mu,\sigma) = \frac{1}{\sigma\sqrt{2\pi}}\exp\left(-\frac{(x-\mu)^2}{2\sigma^2}\right)$$

  - μ represents the mean
  - σ represents the standard deviation

- **GumbelMax:**

$$f(x;\mu,\beta) = \frac{1}{\beta}\exp\left(-\frac{x-\mu}{\beta}\right)\exp\left(-\exp\left(-\frac{x-\mu}{\beta}\right)\right)$$

  - μ represents the location parameter
  - β represents the scale parameter

- **GumbelMin:**

$$f(x;\mu,\beta) = \frac{1}{\beta}\exp\left(\frac{x-\mu}{\beta}\right)\exp\left(-\exp\left(\frac{x-\mu}{\beta}\right)\right)$$

  - μ represents the location parameter
  - β represents the scale parameter

- **GEV:**

$$f(x;\xi,\mu,\sigma) = \frac{1}{\sigma}\left(1+\xi\cdot\frac{x-\mu}{\sigma}\right)^{-1/\xi-1}\exp\left(-\left(1+\xi\cdot\frac{x-\mu}{\sigma}\right)^{-1/\xi}\right)$$

  - ξ represents the shape parameter
  - μ represents the location parameter
  - β represents scale parameter

G Power Matrix

This research builds on the power matrix developed by Alday et al. (2023). To determine power production for each sea-state bin in the power matrix, Alday et al. (2023) (i) formulates the linear heave equation of motion and extracts frequency-dependent hydrodynamic coefficients using a Boundary Element Method (BEM) solver, (ii) solves for the heave response amplitude operator (RAO) $s(\omega)$ and computes the heave response spectrum $S_z(\omega)$, (iii) derives the significant heave amplitude $z_{a1/3}$ and the zero-crossing period T_{2z}, and (iv) calculates the mean absorbed power P for each (H_s, T_e) bin. This subsection provides an overview of these steps and the key assumptions involved.

1. The Corpower C4 wave energy converter is modeled in the frequency domain, considering only heave motion. To define the system's heave response, the following linearized relation is constructed:

$$\left[-\omega^2(m_d + m_a) + i\,\omega\,(b_a + b_{\mathrm{PTO}} + b_v) + c_h\right]\, s(\omega) \;=\; F_e(\omega) \tag{32}$$

   Where:

   - m_d is the dry mass of the device,
   - m_a is the added mass,
   - b_a is the radiation damping
   - b_{PTO} is the damping of the power take off system,
   - b_v is the viscous damping
   - c_h is the hydrostatic stiffness,
   - $s(\omega)$ is the Response Amplitude Operator (RAO),
   - $F_e(\omega)$ is the wave excitation force

   The equation of motion is linearized, meaning that all nonlinear contributions are neglected. The frequency dependent hydrodynamic coefficients $b_a(\omega)$, $m_a(\omega)$ and excitations force $F_e(\omega)$ are obtained from a Boundary Element Method solver (BEM) under deep water assumptions. The hydrostatic stiffness c_h is based on the device's geometry. Finally, the damping of the power take off system b_{PTO} is chosen to maximize power absorption by matching the total system impedance (sub optimal PTO damping law).

2. With all terms in the equation of motion defined, the RAO $s(\omega)$ can be determined. Which represents the amplitude response for each frequency. For each sea state bin (H_s, T_p), the input spectrum $S_\zeta(\omega)$ (measured hindcast spectrum or a JONSWAP fit) is combined with the RAO to define the heave response spectrum, depicted in Equation 33. With the heave response spectrum the zeroth and second moment are determined, noted in Equation 34 and 35.

$$S_z(\omega) = \left|s(\omega)\right|^2 S_\zeta(\omega)\,. \tag{33}$$

$$m_{0z} = \int_0^\infty S_z(\omega)\,\mathrm{d}\omega, \tag{34}$$

$$m_{2z} = \int_0^\infty \omega^2\, S_z(\omega)\,\mathrm{d}\omega. \tag{35}$$

3. The zeroth and second oment yield the significant heave amplitude $z_{a_{1/3}} = 2\sqrt{m_{0z}}$, and the zero-crossing period $T_{2z} = 2\pi\sqrt{\frac{m_{0z}}{m_{2z}}}$.

4. Each sea-state bin (H_s, T_p) is associated with corresponding wave spectrum and heave spectrum response. The mean absorbed power for each bin is calculated using Equation 36, where $\omega_z = 2\pi/T_{2z}$.

$$P = \tfrac{1}{2}\,\omega_z^2\, b_{\mathrm{PTO}}\, z_{a_{1/3}}^2 \tag{36}$$

It is important to recognize that the power matrix is based on several simplifying assumptions about wave climate and device dynamics. These may limit the absolute accuracy of the Corpower C4 inspired power production estimates. However, the matrix still produces consistent power production values that are suitable for comparing different sites rather than for exact power production estimates.

1. **Heave only motion:** Assuming only heave motions simplifies the hydrodynamics. Neglecting surge, pitch and coupling effects can under or over estimate the device's dynamic response.
2. **Neglected interactions:** The wave spring component, pre-tensioning mechanism and the moorings are not included in the formulation of the equation of motion. Ignoring these forces can alter the RAO and response spectra.
3. **Deep water conditions:** BEM derived added mass, damping and excitation forces under deep water conditions may not hold in shallower sites.
4. **Wave climate:** When hindcast spectral data was unavailable, a JONSWAP spectrum $\gamma = 3.3$ was used as a substitute.
5. **Sub optimal PTO damping:** The frequency-dependent PTO damping $b_{\mathrm{PTO}}(\omega)$ is chosen to match the device's intrinsic impedance for maximum mean power absorption.
6. **Unidirectional waves:** Directional spreading is neglected, all wave energy is assumed to propagate along a single direction.

References

[1] Mohammad Mahdi Abaei et al. "Performance evaluation of point-absorber wave energy converters; energy extraction and structural integrity aspects". In: *Ocean Engineering* 317 (2025).

[2] Tunde Aderinto and Hua Li. "Ocean Wave Energy Converters: Status and Challenges". In: *Energies* 11 (2018), p. 26. DOI: 10.3390/en11051250. URL: https://doi.org/10.3390/en11051250.

[3] Tunde Aderinto and Hua Li. "Review on Power Performance and Efficiency of Wave Energy Converters". In: *Energies* 12.4329 (2019), p. 24. URL: https://www.researchgate.net/publication/337262961_Review_on_Power_Performance_and_Efficiency_of_Wave_Energy_Converters.

[4] George Biddell Airy. "Tides and Waves". In: *Encyclopaedia Metropolitana, Mixed Sciences*. Ed. by Hugh James Rose et al. London: Rodwell & Martin, 1841.

[5] Hirotugu Akaike. "Information theory and an extension of the maximum likelihood principle". In: *Proceedings of the 2nd International Symposium on Information Theory*. Ed. by B. N. Petrov and F. Csáki. Akademiai Kiado, 1973, pp. 267–281.

[6] Matías Alday and George Lavidas. "The ECHOWAVE Hindcast: A 30-years high resolution database for wave energy applications in North Atlantic European waters". In: *Renewable Energy* 236 (2024). DOI: 10.1016/j.renene.2024.121391. URL: https://www.tudelft.nl/ceg/mrel.

[7] Matias G. Alday, Vaibhav Raghavan, and George Lavidas. "Analysis of the North Atlantic offshore energy flux from different reanalysis and hindcasts". In: *Proceedings of the European Wave and Tidal Energy Conference*. Vol. 15. Article 140. EWTEC, 2023. DOI: 10.36688/ewtec-2023-140. URL: https://doi.org/10.36688/ewtec-2023-140.

[8] M. Alves. "Frequency-Domain Models". In: *Numerical Modelling of Wave Energy Converters*. Ed. by A.F.O. Falcão and J.C.C. Henriques. Elsevier, 2016. DOI: 10.1016/B978-0-12-803210-7.00002-5.

[9] Matthieu Ancellin and Frédéric Dias. "Capytaine: a Python-based linear potential flow solver". In: *Journal of Open Source Software* 4.36 (Apr. 2019), p. 1341. DOI: 10.21105/joss.01341. URL: https://doi.org/10.21105%2Fjoss.01341.

[10] Clive W. Anderson. "The Aggregate Excess Measure of Severity of Extreme Events". In: *Journal of Research of the National Institute of Standards and Technology* 99.4 (1994), pp. 555–561.

[11] A. Azam et al. "Knowledge structuring for enhancing mechanical energy harvesting (MEH): an in-depth review from 2000 to 2020 using CiteSpace". In: *Renewable and Sustainable Energy Reviews* 150 (2021). DOI: 10.1016/j.rser.2021.111460.

[12] Aurélien Babarit and Gérard Delhommeau. "Theoretical and numerical aspects of the open source BEM solver NEMOH". In: *Proceedings of the 11th European Wave and Tidal Energy Conference (EWTEC2015)*. Nantes, France, 2015.

[13] Arnob Barua and Md Salauddin Rasel. "Advances and challenges in ocean wave energy harvesting". In: *Sustainable Energy Technologies and Assessments* 61 (2024). URL: https://www.sciencedirect.com/science/article/pii/S2213138824000035.

[14] Silvia Bozzi, Renata Archetti, and Giuseppe Passoni. "Wave electricity production in Italian offshore: A preliminary investigation". In: *Renewable Energy* 62 (2014), pp. 407–416. ISSN: 0960-1481. DOI: https://doi.org/10.1016/j.renene.2013.07.030. URL: https://www.sciencedirect.com/science/article/pii/S0960148113003856.

[15] *On the Long-Term Reliability Analysis of a Point Absorber Wave Energy Converter*. Vol. Volume 10: Ocean Renewable Energy. International Conference on Offshore Mechanics and Arctic Engineering. June 2017, V010T09A024. DOI: 10.1115/OMAE2017-62141. eprint: https://asmedigitalcollection.asme.org/OMAE/proceedings-pdf/OMAE2017/57786/V010T09A024/2534932/v010t09a024-omae2017-62141.pdf. URL: https://doi.org/10.1115/OMAE2017-62141.

[16] R. Carballo and G. Iglesias. "A methodology to determine the power performance of wave energy converters at a particular coastal location". In: *Energy Conversion and Management* 61 (2012), pp. 8–18.

[17] O. Choupin et al. "Premises for an annual energy production and capacity factor improvement towards a few optimised wave energy converters configurations and resources pairs". In: *Applied Energy* 312 (2022), pp. 1–29. DOI: 10.1016/j.apenergy.2022.118716. URL: https://doi.org/10.1016/j.apenergy.2022.118716.

[18] Ryan Coe, Yi Hsiang, and Jennifer van Rij. "A Survey of WEC Reliability, Survival and Design Practices". In: *Energies* 11.4 (2018). Accessed: 17-Feb-2025, pp. 1–19. DOI: 10.3390/en11010004. URL: https://www.mdpi.com/1996-1073/11/1/4.

[19] Ryan G. Coe et al. "Maybe less is more: Considering capacity factor, saturation, variability, and filtering effects of wave energy devices". In: *Applied Energy* 291 (2021), p. 116763. DOI: 10.1016/j.apenergy.2021.116763. URL: https://doi.org/10.1016/j.apenergy.2021.116763.

[20] CorPower Ocean. *CorPower C4 - Wave Energy Converter*. 2025. URL: https://corpowerocean.com.

[21] J. Cruz. *Ocean Wave Energy: Current Status and Future Perspectives*. Berlin/Heidelberg, Germany: Springer Science & Business Media, 2007.

[22] Samuel J. Edwards and Ryan G. Coe. "The Effect of Environmental Contour Selection on Expected Wave Energy Converter Response". In: *Journal of Offshore Mechanics and Arctic Engineering* 141.1 (Aug. 2018), p. 011901. ISSN: 0892-7219. DOI: 10.1115/1.4040834. eprint: https://asmedigitalcollection.asme.org/offshoremechanics/article-pdf/141/1/011901/6375365/omae_141_01_011901.pdf. URL: https://doi.org/10.1115/1.4040834.

[23] Ember. *European Electricity Review 2024: EU Electricity Trends*. Accessed: February 17, 2025. 2024. URL: https://ember-energy.org/latest-insights/european-electricity-review-2024/eu-electricity-trends/.

[24] Energy Club TU Delft. *Ocean Energy*. Accessed: 17-Feb-2025. 2025. URL: https://energyclub.nl/de-pillars/ocean-energy.

[25] Energy Institute, KPMG, and Kearney. *Statistical Review of World Energy - 73rd Edition*. 2024. URL: https://www.energyinst.org/statistical-review.

[26] European Commission. *2030 Climate Targets*. n.d. URL: https://climate.ec.europa.eu/eu-action/climate-strategies-targets/2030-climate-targets_en.

[27] European Commission. *2040 Climate Target*. 2024. URL: https://climate.ec.europa.eu/eu-action/climate-strategies-targets/2040-climate-target_en.

[28] European Parliament. *Offshore Renewable Energy: The European Green Deal*. 2020.

[29] Francesco Ferri et al. "Balancing Power Output and Structural Fatigue of Wave Energy Converters by Means of Control Strategies". In: *Energies* 7 (2014), pp. 2246–2273. URL: https://doi.org/10.3390/en7042246.

[30] Bingyong Guo and John V. Ringwood. "A review of wave energy technology from a research and commercial perspective". In: *IET Renewable Power Generation* 15 (2021). URL: https://ietresearch.onlinelibrary.wiley.com/doi/10.1049/rpg2.12302.

[31] Bingyong Guo et al. "A Review of Point Absorber Wave Energy Converters". In: *Journal of Marine Science and Engineering* 10.10 (2022).

[32] Jorgen Hals et al. "Tank testing of an inherently phase-controlled wave energy converter". In: *International Journal of Marine Energy* 15 (2016). Selected Papers from the European Wave and Tidal Energy Conference 2015, Nantes, France, pp. 68–84. DOI: 10.1016/j.ijome.2016.04.007. URL: https://www.sciencedirect.com/science/article/pii/S2214166916300182.

[33] Intergovernmental Panel on Climate Change. *Renewable Energy Sources and Climate Change Mitigation: Special Report of the Intergovernmental Panel on Climate Change*. Ed. by Ottmar Edenhofer et al. Accessed: February 17, 2025. Cambridge, United Kingdom and New York, NY, USA: Cambridge University Press, 2012. ISBN: 978-1-107-02340-6. URL: https://www.cambridge.org/9781107607101.

[34] E. Katsidoniotaki et al. "Loads on a Point-Absorber Wave Energy Converter in Regular and Focused Extreme Wave Events". In: *Ocean Renewable Energy* 9 (2020). DOI: 10.1115/omae2020-18639. URL: https://doi.org/10.1115/omae2020-18639.

[35] Eirini Katsidoniotaki et al. "Reduced order modeling of wave energy systems via sequential Bayesian experimental design and machine learning". In: *Applied Ocean Research* 155 (2025), p. 104439. ISSN: 0141-1187. DOI: 10.1016/j.apor.2025.104439. URL: https://doi.org/10.1016/j.apor.2025.104439.

[36] Harald E. Krogstad and Øivind A. Arntsen. *Linear Wave Theory Part A: Regular Waves*. Tech. Rep. Norwegian University of Science and Technology, Trondheim, Norway, 2010.

[37] G Lavidas et al. "Effects of metocean conditions on selecting optimal location for wave energy production". In: *Proceedings of the 11th European Wave and Tidal Energy Conference (EWTEC)* 1906 (2021), pp. 1–10.

[38] George Lavidas. "Selection index for Wave Energy Deployments (SIWED): A near-deterministic index for wave energy converters". In: *Energy* 196 (2020), pp. 1–14. DOI: 10.1016/j.energy.2020.117131. URL: https://doi.org/10.1016/j.energy.2020.117131.

[39] C.F. Lee et al. "Extreme response analysis of a floating vertical axis wind turbine based on modified environmental contour method". In: *Ocean Engineering* 270 (2023), p. 113459.

[40] L. Li et al. "Investigation on long-term extreme response of an integrated offshore renewable energy device with a modified environmental contour". In: *Renewable Energy* 132 (2019), pp. 33–42.

[41] Q. Li, Z. Gao, and T. Moan. "Modified environmental contour method to determine the long-term extreme responses of a semi-submersible wind turbine". In: *Ocean Engineering* 142 (2017), pp. 563–576.

[42] X. Li and W. Zhang. "Long-term assessment of a floating offshore wind turbine under environmental conditions with multivariate dependence structures". In: *Renewable Energy* 147 (2020), pp. 746–775.

[43] Xuan Li and Wei Zhang. "Long-term fatigue damage assessment for a floating offshore wind turbine under realistic environmental conditions". In: *Renewable Energy* 159 (2020), pp. 570–584.

[44] Francesco De Marinis. "Advancements in Wave Energy Conversion: A Numerical Analysis of the C4 CorPower WEC's Dynamic Response in Various Wave Scenarios". MA thesis. Politecnico di Torino, 2023/2024.

[45] Metocean API Contributors. *Metocean API Documentation*. Read the Docs. May 8, 2025. URL: `https://metocean-api.readthedocs.io/en/latest/index.html` (visited on 05/08/2025).

[46] G. Mork et al. "Assessing the global wave energy potential". In: *Proceedings of the ASME 2010 29th International Conference on Ocean, Offshore and Arctic Engineering*. Shanghai, China, 2010.

[47] M.A. Mustapa et al. "Wave energy device and breakwater integration: A review". In: *Renewable and Sustainable Energy Reviews* 77 (2017). DOI: 10.1016/j.rser.2017.03.110.

[48] Georges Chapalain Nicolas Guillou. "Annual and Seasonal Variabilities in the Performances of Wave Energy Converters". In: *Elsevier* 165 (2018), pp. 812–823. DOI: 10.1016/j.energy.2018.10.001. URL: https://doi.org/10.1016/j.energy.2018.10.001.

[49] Norton Rose Fulbright. *The EU Green Deal Explained*. https://www.nortonrosefulbright.com/en/knowledge/publications/c50c4cd9/the-eugreen-deal-explained. 2020.

[50] Ocean Energy Europe. *2030 Ocean Energy Vision: Industry ambitions for a blue economy*. https://www.oceanenergy-europe.eu/wp-content/uploads/2020/10/OEE_2030_Ocean_Energy_Vision.pdf. 2020.

[51] J. Orszaghova et al. "Variability of Wave Power Production of the M4 Machine at Two Energetic Open Ocean Locations: off Albany, Western Australia and at EMEC, Orkney, UK". In: *Renewable Energy* (2022), p. 27. DOI: 10.48550/arXiv.2210.13807. URL: https://arxiv.org/abs/2210.13807.

[52] Bruno Paduano et al. "Towards standardised design of wave energy converters: A high-fidelity modelling approach". In: *Renewable Energy* 224 (2024).

[53] pyvinecopulib. *pyvinecopulib: A Python wrapper for vinecopulib*. https://github.com/vinecopulib/pyvinecopulib. Accessed: 2025-04-18. 2019.

[54] B. Reguero, I. Losada, and F. Méndez. "A global wave power resource and its seasonal, interannual and long-term variability". In: *Applied Energy* 148 (2015), pp. 366–380. DOI: 10.1016/j.apenergy.2015.03.114. URL: https://doi.org/10.1016/j.apenergy.2015.03.114.

[55] Gordon Reikard, Bryson Robertson, and Jean-Raymond Bidlot. "Combining wave energy with wind and solar: Short-term forecasting". In: *Renewable Energy* 81 (2015), pp. 442–456. DOI: 10.1016/j.renene.2015.03.032. URL: https://www.sciencedirect.com/science/article/pii/S0960148115002141.

[56] H. Santo, P. Taylor, and P. Stansby. "The performance of the three-float M4 wave energy converter off Albany, on the south coast of Western Australia, compared to Orkney (EMEC) in the U.K." In: *Renewable Energy* 146 (2020), pp. 444–459. DOI: 10.1016/j.renene.2019.06.146. URL: https://doi.org/10.1016/j.renene.2019.06.146.

[57] Zahra Shahroozi et al. "Environmental design load for the line force of a point-absorber wave energy converter". In: *Applied Ocean Research* 128 (2022), p. 103305. DOI: 10.1016/j.apor.2022.103305. URL: https://www.sciencedirect.com/science/article/pii/S0141118722001164.

[58] Charles Spearman. "The proof and measurement of association between two things". In: *American Journal of Psychology* 15.1 (1904), pp. 72–101.

[59] A. Subbulakshmi et al. "Recent advances in experimental and numerical methods for dynamic analysis of floating offshore wind turbines—An integrated review". In: *Renewable and Sustainable Energy Reviews* 164 (2022). Article number 112525, p. 112525.

[60] Philipp R. Thies et al. "Mooring line fatigue damage evaluation for floating marine energy converters: Field measurements and prediction". In: *Renewable Energy* 63 (Mar. 2014), pp. 133–144. DOI: 10.1016/j.renene.2013.08.050.

[61] Hendrik L Tolman. *The numerical model WAVEWATCH: a third generation model for hindcasting of wind waves on tides in shelf seas*. Faculty of Civil Engineering, Delft University of Technology, 1989.

[62] Nathan Tom. *Review of Wave Energy Converter Power Take-Off Systems, Testing Practices, and Evaluation Metrics*. Preprint NREL/CP-5700-82807. National Renewable Energy Laboratory, 2022. URL: https://www.nrel.gov/docs/fy23osti/82807.pdf.

[63] United Nations. *Causes and Effects of Climate Change*. 2025. URL: https://www.un.org/en/climatechange/science/causes-effects-climate-change.

[64] United Nations Environment Programme (UNEP) and Partners. *The Production Gap Report 2019*. 2019. URL: https://productiongap.org/wp-content/uploads/2019/11/Production-Gap-Report-2019.pdf.

[65] Valentina Vannucchi and Lorenzo Cappietti. "Wave Energy Assessment and Performance Estimation of State of the Art Wave Energy Converters in Italian Hotspots". In: *Sustainability* 8 (2016).

[66] A. Wahyudie et al. "Simple bottom-up hierarchical control strategy for heaving wave energy converters". In: *International Journal of Electrical Power & Energy Systems* 87 (2017).

[67] D.S. Wilks. "Chapter 4 - Parametric Probability Distributions". In: *Statistical Methods in the Atmospheric Sciences*. Ed. by Daniel S. Wilks. Vol. 100. International Geophysics. Academic Press, 2011, pp. 71–131. DOI: https://doi.org/10.1016/B978-0-12-385022-5.00004-X. URL: https://www.sciencedirect.com/science/article/pii/B978012385022500004X.

[68] S. R. Winterstein et al. "Environmental Parameters for Extreme Response: Inverse FORM with Omission Factors". In: *Proceedings of the 6th International Conference on Structural Safety and Reliability (ICOSSAR-93)*. Innsbruck, Austria, 1993.

[69] Xinyu Yuan et al. "Fatigue Load Modeling of Floating Wind Turbines Based on Vine Copula Theory and Machine Learning". In: *Journal of Marine Science and Engineering* 12.26 (2024).

[70] Yuliang Zhao and Sheng Dong. "Multivariate probability analysis of wind-wave actions on offshore wind turbine via copula-based analysis". In: *Ocean Engineering* 288 (2023), pp. 2–16. DOI: 10.1016/j.oceaneng.2023.116071. URL: https://www.elsevier.com/locate/oceaneng.

[71] Binzhen Zhou et al. "Optimal strategy of the asymmetric wave energy converter survival in extreme waves". In: *Physics of Fluids* 36.5 (2024). URL: https://doi.org/10.1063/5.0208825.